Bulletin of Mathematical Biology (2025) 87:45
https://doi.org/10.1007/s11538-025-01425-1

Society for Mathematical Biology

ORIGINAL ARTICLE

Influence of Contact Lens Parameters on Tear Film Dynamics

Darshan Ramasubramanian[1,2] · José Luis Hernández-Verdejo[1] · José Manuel López-Alonso[1]

Received: 1 August 2024 / Accepted: 3 February 2025

Abstract
This study employs a computational model to simulate the dynamics of tear fluid and tear film in conjunction with contact lens motion, examining the interplay between diverse contact lens characteristics—such as material, design, and dimensions—and key ocular factors like dry eye conditions, corneal size, and blink rate. These interactions are critical for customising lens fit to maximise wearer comfort. Utilising optical measurements from a single participant, the study integrates data on tear meniscus size, blink velocity, and palpebral fissure height with sixteen different contact lens parameters, including Young's modulus, thickness, diameter, and curvature. Correlation analyses were conducted to determine the impact of these parameters on the dynamics of the tear fluid and overall tear film. Results show that the diameter and Young's modulus of the contact lens significantly influence pre-lens tear film thickness, with robust, statistically significant correlations. In contrast, lens thickness and base curve showed minimal impact, as evidenced by weak and non-significant correlations. These findings underscore the critical roles of lens diameter and Young's modulus in enhancing the stability and distribution of tear fluid, thereby improving wearer comfort and advancing contact lens design.

Keywords Contact lens design · Tear fluid · Tear film dynamics · Correlation analysis · Wearer comfort

1 Introduction

Selecting and fitting a contact lens (CL) is a nuanced process that profoundly impacts ocular health, requiring a comprehensive evaluation of lens material, mechanics, and

✉ José Manuel López-Alonso
jmlopez@ucm.es

1 Faculty of Optics and Optometry, Complutense University of Madrid, Madrid, Spain

2 Alain Afflelou Óptico, Portugal, Av. António Augusto de Aguiar, 11, 1050-016 Lisbon, Portugal

Published online: 19 February 2025

surface characteristics—such as lubrication, friction, and wetness (Hart et al. 2020). With numerous people wearing CLs these days, design factors, including corneal coverage, lens parameters, movement, tear exchange, and wear schedule, become critical not only to the comfort of CL wearers but also to the effectiveness of the lens and overall eye health. The subjective nature of comfort, coupled with variability among wearers, underscores the complexity of optimising CL usage to meet individual needs and ensure optimal ocular health.

At the heart of this optimisation is the human tear film, a multi-layered structure that plays a vital role in maintaining ocular health and ensuring clear vision. This film, with its layers of mucin, aqueous, and lipid, ranges in thickness from 2 to 5.5 μm and is pivotal for providing moisture, protection, and a clear refractive surface (King-Smith et al. 2004; Paranjpe et al. 2019). The insertion of a CL introduces a dynamic alteration in the tear film, segmenting it into the pre-lens (PLTF) and post-lens tear films (PoLTF), which in turn influences the behaviour and distribution of the tear film, especially during blinking (Nichols and King-Smith 2003). When delving into the specifics of CL interaction with the tear film, it is noted that CLs significantly alter the structure of the tear film, creating the PLTF and PoLTF, with the CL itself being markedly thicker than these tear film layers (Wang et al. 2003). The blinking process, orchestrated by the 'lid wiper' action of the upper eyelid (Jones et al. 2008), is integral to spreading the tear film, thus affecting lens comfort and the health of the ocular surface.

To gain an in-depth understanding of the interactions between CLs, blinking, and the tear film, researchers employ mathematical models, incorporating non-linear partial differential equations, that illuminate the dynamics of the tear film (Braun 2012). These models examine aspects such as volume changes, evaporation rates, and the detailed interactions driven by eyelid movements (Braun 2003; Jones et al. 2005; Braun and King-Smith 2007; Heryudono et al. 2007). They integrate specific CL-related parameters to uncover how the material and geometric characteristics of the CL affect tear film behaviour (Chauhan and Radke 2001; Anderson et al. 2021). Emphasising the significance of lubrication regimes and frictional forces, these models are pivotal in predicting the complex interplay among CLs, eyelids, and the tear film (Dunn et al. 2013). However, it is important to acknowledge that these models depend on certain assumptions, including the prevalent flat cornea approximation and the treatment of the tear film as a Newtonian fluid, despite its complexity (Braun 2003). Addressing the vital roles of surface tension and viscosity is crucial, as these factors demand sophisticated modelling techniques to accurately depict the intricate dynamics of the tear film (Tiffany et al. 1989; Tiffany 1991).

Following the exploration of tear film dynamics and the assumptions underlying mathematical models, it is imperative to delve into the mechanics of blinking—an essential, semi-autonomous eyelid movement critical for distributing tears, ensuring lubrication, and aiding tear drainage (Espinosa et al. 2018). The blink cycle comprises four distinct phases (Braun et al. 2015): the downstroke (closing phase), a moment when the upper eyelid turns without touching the lower eyelid (eye closed or turning point), the upstroke (opening phase), and the upper eyelid returning to its original position (eye is fully open). Numerous studies have employed high-speed cameras to analyse different blinking models, enhancing the understanding of tear film behaviour

during these phases. Initial models focused on the upstroke (Jones et al. 2005), subsequently expanding to encompass the full spectrum of eyelid motions, including sinusoidal and realistic movements (Braun and King-Smith 2007; Heryudono et al. 2007). Understanding the distinction between complete and partial blinks is essential; complete blinks promote even tear distribution and prevent evaporation, while partial blinks, often seen in individuals with dry eye or frequent digital device users, can compromise tear film quality (Braun et al. 2015). This distinction is especially relevant for CL wearers, as rapid eyelid movements can impact the stability and distribution of the tear film. Computational models that integrate these aspects of blinking, particularly focusing on the vertical movements of the CL (Chauhan and Radke 2001), help predict how these forces affect the lens in various directions. Assuming a constant PoLTF thickness allows for precise measurement of the PLTF thickness (Anderson et al. 2021), offering insights into the interplay between blinking dynamics and CL usage.

Building upon the understanding of blinking dynamics and their influence on tear film behaviour, it is pertinent to consider the adaptability of mathematical models to individual ocular health. Enhancing the precision of these models involves incorporating real subject parameters, obtainable through advanced measurement techniques. For example, employing Optical Coherence Tomography allows for precise determination of tear meniscus measurements (Garhöfer et al. 2020), illustrating how these tailored parameters can refine the analyses. Integrating such specific data enables a more nuanced understanding of individual variations in critical tear film attributes like viscosity and surface tension (Tiffany et al. 1989; Tiffany 1991), and how these variations affect CL interaction. This approach to personalised modelling is crucial for predicting the comfort and ocular health implications of CL wear, ensuring that analyses are customised to reflect the unique characteristics of eyes of everyone.

Following the integration of real subject parameters to enhance the precision of computational models for ocular health, this study employs descriptive statistics to further refine the understanding of tear film dynamics. Central to this analysis are measures of central tendency, variability, and distribution (Kaur et al. 2018), which encapsulates the dynamics of PLTF thickness through essential metrics such as mean, standard deviation, skewness, and kurtosis. The mean PLTF thickness is particularly vital, serving as an indicator of ocular surface hydration and lens functionality (Kaur et al. 2018; Capote-Puente et al. 2023). The standard deviation highlights the uniformity or variability of the tear film, impacting its effectiveness as a lubricant and protective barrier. Meanwhile, skewness and kurtosis provide more profound insights into the asymmetrical and peaked nature of tear film distribution (Kim 2013; Iyamu and Enobakhare 2019), which are pivotal for clinical assessments and the design of CLs. This approach ensures that the analysis not only accounts for individual variations but also enhances the predictive accuracy regarding the comfort and health implications of CL wear.

Building on the foundational analysis of tear film dynamics, this study employs correlation analysis to further investigate the effects of various CL parameters on tear film behaviour (Miot 2018; Lee et al. 2020). This statistical approach effectively quantifies the strength and directionality of relationships between two variables, offering crucial

insights without asserting causation. Particularly useful in observational studies, correlation analysis helps to uncover the interdependencies among variables, facilitating hypothesis development and directing subsequent research efforts (Miot 2018). By applying this methodology, the study gains a deeper understanding of how CL motion influences PLTF dynamics. This knowledge is critical for enhancing CL design and optimising wearer comfort and ocular health outcomes, ensuring that innovations in CL technology are both effective and tailored to meet diverse user needs.

This study advances personalised modelling by applying a mathematical model that simulates the dynamics of the tear film in conjunction with CL motion, customised for individual subjects (Anderson et al. 2021). By adjusting the material and geometric properties of the CLs, it aims to precisely analyse the impact of these parameters on tear film behaviour. The research utilises descriptive statistics and correlation analysis to methodically evaluate the interactions between CL properties and tear film dynamics. Specifically, the study explores the complex relationships between CL parameters such as Young's modulus, base curve, diameter, and thickness, and PLTF dynamics metrics including mean, standard deviation, skewness, and kurtosis. This comprehensive examination seeks to determine how alterations in CL design affect the behaviour and distribution of the tear film on the ocular surface, elucidating the influence of lens physical properties on tear film stability and enhancing ocular comfort.

The subsequent section outlines the methodology used to analyse tear film and blink dynamics, explaining how the model can be adapted to accommodate individual subjects and several types of CLs. It will also cover the descriptive statistics and data distribution of PLTF thickness utilised in this study. The findings from this tailored approach will be presented in the third section, which will detail the impact of various CL parameters on PLTF dynamics. Following the results, a comprehensive discussion and conclusion will synthesise these insights, exploring their wider implications for ocular health and CL design.

2 Materials and Methods

This section explores the mathematical model by Anderson et al. (2021), which sheds light on the complex interactions between blinking, CL wear, and tear film dynamics. It also addresses how subject-specific parameters, along with the material and geometric properties of the CL, are incorporated into the model. This incorporation facilitates the development of personalised models, enabling an accurate representation of individual tear film behaviour in the context of CL usage, enhancing the understanding of the factors that influence tear film dynamics.

2.1 Mathematical Modelling of Tear Film Dynamics with Blinking and CL Motion

Figure 1 illustrates the dynamics of the tear film for CL wearers, as described by Anderson et al. (2021). The palpebral fissure half-width (L) is modified based on previous research to represent a specific characteristic of an individual, while the typical tear film thickness (d) is set at a distance from the menisci. The length scale

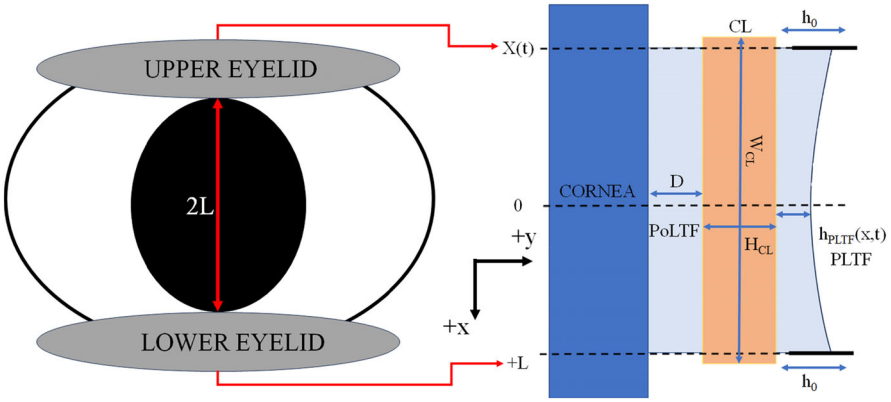

Fig. 1 Schematic diagram of the eye with the tear film dynamics for CL wearers. The parameters described in this figure are mentioned in the text

ratio is given as $\epsilon = d/L << 1$, simplifying the problem to solving a nonlinear partial differential equation for the tear film thickness. The velocity components in the x and y directions are denoted as $U = (u, v)$. At the leading order, the conservation of mass and momentum in the x and y directions characterises the parallel flow problem, underpinning the fundamental dynamics of the model. During a blink, the upper eyelid moves vertically while the lower eyelid remains stationary at $x = +L$, and the position of the upper eyelid varies with time, represented as $x = X(t)$. The centre of the eye is considered as $x = 0$, with the total eyelid span being $2L$. The maximum blink speed (U_m) is influenced by the closing phase of the blink cycle, which varies according to the blinking characteristics of an individual. The time scale for real blink speeds is L/U_m. The thickness of the PLTF is indicated by $h_{PLTF}(x, t)$ (or $h(x, t)$ for simplification), while the tear meniscus height is noted as h_0. The derivation of the mathematical model employed the following properties: viscosity (μ), density (ρ), surface tension (σ_0) and gravitational acceleration (g). The next subsection will provide a comprehensive discussion of the parameters mentioned, encompassing both subject-specific factors and tear film characteristics.

The non-dimensionalities involve scaling variables using dimensional quantities denoted by a "*", which is exemplified in Eq. 1, illustrating the transformation of the variables of the model into a non-dimensional form, which is given by the governing equations of the leading contributions from lubrication theory on $0 \leq y \leq h^*(x, t)$ and $X^*(t) \leq x^* \leq +L$ (Heryudono et al. 2007; Anderson et al. 2021). The non-dimensional domain is in the form $0 \leq y \leq h(x, t)$ and $X(t) \leq x \leq 1$.

$$
\begin{aligned}
&x^* = Lx; h^* = dh; t^* = \frac{L}{U_m}t; u^* = U_m u; v^* = \varepsilon U_m v \\
&X^* = LX; U_s^* = U_m U_s; X_{cl}^* = LX_{cl}; U_{cl}^* = U_m U_{cl} \\
&G = \frac{\rho g d^2}{\mu U_m}; Ca = \frac{\mu U_m}{\sigma \varepsilon^3}
\end{aligned}
\tag{1}
$$

The fluid pressure (p) is influenced by the interface curvature and tear film parameters, as detailed in Eq. 2. Ca in the fluid pressure equation represents the Capillary number.

$$p = -\frac{\varepsilon^3}{Ca}\frac{\partial^2 h}{\partial x^2} \tag{2}$$

Equation 3 illustrates the volume flux (q) and the tangential velocity at the free surface modulated by the position and velocity of the upper eyelid (U_s).

$$\begin{aligned} q &= \frac{h^3}{12}\left(1 + \frac{3\beta_{cl}}{h + \beta_{cl}}\right)\left(-\frac{\partial p}{\partial x} + G\right) + \frac{h}{2}\left(1 + \frac{\beta_{cl}}{h + \beta_{cl}}\right)(U_s - U_{cl}) + hU_{cl} \\ U_s &= \frac{1 - x}{1 - X(t)}\frac{dX}{dt} \end{aligned} \tag{3}$$

The slip coefficient specific to the CL is denoted by β_{cl}, which characterises the slip boundary condition at the CL interface. Equation 4 describes the change in PLTF thickness over time, directly proportional to the negative volume flux gradient across the space.

$$\frac{\partial h}{\partial t} = -\frac{\partial q}{\partial x} \tag{4}$$

Boundary conditions correspond to the tear meniscus height, enforcing zero flux at the boundaries relative to the lid motion ($Q_{top} = Q_{bot} = 0$), as illustrated in Eq. 5. A polynomial function is utilised as the initial condition, also described in Eq. 5.

$$\begin{aligned} &q_{up} = -\frac{dX}{dt}h_0 + Q_{top}; q_{low} = -Q_{bot} \\ &h(1, t) = h(X(t), t) = h_0 \\ &h(x, 0) = h_{\min} + (h_0 - h_{\min})x^m \end{aligned} \tag{5}$$

where h_{min} is the value determined by equating it to the desired dimensionless volume with an even value of m (for most cases, m = 4) (Braun and King-Smith 2007; Heryudono et al. 2007). Equation 6 presents the initial dimensionless volume ($V_i = 8$,) formula, which is used to determine the value of h_{min} based on the initial position of the upper eyelid, the tear meniscus height (h_0), and the parameter m (Anderson et al. 2021).

$$V_i = \frac{1 - X(0)}{m + 1}[mh_{\min} + h_0] \tag{6}$$

Equation 7 represents the motion of the upper eyelid, which is modelled as a sinusoidal function where λ indicates the proportion of the eye that remains open, and ω_{blink} is the non-dimensional blink frequency, which is set to 1 to denote that a complete blink cycle corresponds to $2\pi/\omega_{blink}$. For a complete blink, λ is set to 0.1,

reflecting that the upper and lower eyelids do not completely touch, leaving 10% of the eye open at the peak of closure. In scenarios representing half blinks, the eyelid only completes half its motion, corresponding to $\lambda = 0.5$, before the eye opens.

$$\begin{aligned} X(t) &= [-\lambda + (1-\lambda)\cos(\omega_{blink}t)] \\ X\prime(t) &= [-(1-\lambda)\sin(\omega_{blink}t)] \end{aligned} \tag{7}$$

2.1.1 CL Motion Equations

The mathematical framework used to analyse tear film dynamics, which examines the interaction between blinking and CL movement, is based on the seminal research by Anderson et al. (2021). A detailed derivation of this framework can be found in the referenced citation and summarised in this section. Adhering to Newton's second law, the dynamics of the superior-inferior motion of the CL equates the acceleration of the CL to the result of the total forces acting on it, as described in Eq. 8.

$$M\frac{dU_{cl}}{dt} = F^*_{PoLTF} + F^*_{uplid} + F^*_{lowlid} + F^*_{PLTF} + F^*_{elastic} \tag{8}$$

where M is the mass of the CL, and the dimensional forces are represented with "*". The dimensional viscous force of the PoLTF (F^*_{PoLTF}), accounts for the fluid dynamics between the CL and the cornea, explicitly incorporating the area of the CL. The fluid interaction in the gap between the eyelids and the CL is modelled by considering the regions of fluid influenced by blinking dynamics, represented by the dimensionless forces F^*_{uplid} and F^*_{lowlid}. The dimensional PLTF viscous force (F^*_{PLTF}) describes the fluid interaction between the CL and the external environment, which is heavily influenced by the dynamics of the lipid layer in the tear film. These dimensional forces are scaled by multiplying them with $L^3/MU_m d$ to convert them into non-dimensional viscous forces, simplifying the model and aiding in comparative analysis.

Additionally, the centring elastic force ($F^*_{elastic}$) is always directed to promote the alignment and centring of the CL on the cornea. The non-dimensional elastic force ($F_{elastic}$) is obtained by normalizing the dimensional elastic force with the inertial force. Equation 9 defines the non-dimensional PoLTF force (F_{PoLTF}), while Eqs. 10 and 11 describe the non-dimensional forces acting within the gap between the CL and the eyelids (F_{uplid}, F_{lowlid}). The non-dimensional PLTF force (F_{PLTF}) is outlined in Eqs. 12 and 13 provides the definition of the non-dimensional elastic force ($F_{elastic}$).

$$F_{PoLTF} = F_V\left[-\frac{A_{cl}}{D + \beta_{cl} + \beta_{eye}}U_{cl}\right] \tag{9}$$

$$F_{uplid} = F_V\left[\frac{A_{uplid}(t)}{h_{lid} + \beta_{cl} + \beta_{lid}}\left(\frac{dX}{dt} - U_{cl}\right)\right] \tag{10}$$

$$F_{lowlid} = F_V\left[-\frac{A_{lowlid}(t)}{h_{lid} + \beta_{cl} + \beta_{lid}}U_{cl}\right] \tag{11}$$

$$F_{PLTF} = F_V \left[W_{cl} \int_X^1 \frac{U_s - U_{cl}}{h + \beta_{cl}} dx \right] \tag{12}$$

$$F_{elastic} = -F_E sign\left(X_{cl} - X_{eye}\right) \tag{13}$$

where F_V and F_E represent the dimensionless viscous and elastic forces, respectively. D denotes the PoLTF thickness while A_{cl} is the area of the CL. $A_{uplid}(t)$ and $A_{lowlid}(t)$ represent the areas of the CL covered by the upper eyelid and lower eyelid, respectively. X_{cl} and U_{cl} correspond to the position and the velocity of the upper eyelid, respectively, while h_{lid} denotes the constant thickness of the fluid layer between the CL and the eyelids. Finally, X_{eye} represents the position of the eye, which is assumed to remain stationary during blinking ($X_{eye} = 0$). The slip coefficients, β_{cl}, β_{eye} and β_{lid}, correspond to the CL, the corneal surface, and the eyelids, respectively. It is assumed that there is no slip between the tear film and the eyelids or the corneal surface, indicating that the tear film adheres fully to these surfaces ($\beta_{eye} = \beta_{lid} = 0$). However, the CL exhibits relative motion concerning the tear film and, therefore, a slip coefficient of $\beta_{cl} = 0.01$ is applied.

The elastic centring force ($F_{elastic}$) is integrated to facilitate the alignment of the CL, which is influenced by the peripheral pressure on the sclera and CL-specific properties such as the elastic modulus (ϵ_m), a Poisson ratio ($\nu = 0.49$), and the CL geometric parameters such as thickness (H_{cl}), diameter (W_{cl}), and radius of curvature (R_{cl}). The dimensional magnitude of the elastic force (F_e) is described in Eq. 14, while the assumed constant elastic energy per unit area (E) is defined in Eq. 15, where the sine of the semi-angle of the lens (θ) is expressed as ($\sin(\theta) = W_{cl}/2R_{cl}$). Further expansion of the elastic centring force reveals that the dimensional elastic force (F_e) is directly proportional to Young's modulus, thickness, and diameter while being inversely proportional to the base curve, as outlined in Eq. 16.

$$F_e = 2R_{cl} E \sin(\theta) \tag{14}$$

$$E = \frac{1}{12} \frac{\varepsilon_m H_{cl}^3}{1 - \nu} \left(\frac{1}{R_{cl}} - \frac{1}{R_{sc}} \right)^2 \tag{15}$$

$$F_e = \left[\frac{W_{cl}}{12} \frac{\varepsilon_m H_{cl}^3}{1 - \nu} \left(\frac{1}{R_{cl}} - \frac{1}{R_{sc}} \right)^2 \right] \tag{16}$$

Equation 17 defines the mass of the CL as the product of its density and volume.

$$M = \rho_{cl} \pi \left(\frac{W_{cl}}{2} \right)^2 H_{cl} \tag{17}$$

Expanding the non-dimensional viscous and elastic forces offers a detailed insight into the influence of each CL parameter on its motion. The non-dimensional viscous force (F_V), defined in Eq. 18, can be defined as the ratio of the dimensional viscous

force ($\mu U_m L/d$) and the inertial force (MU_m^2/L), which is inversely proportional to both the CL diameter and thickness. In contrast to the dimensional elastic force (F_e) shown in Eq. 16, the non-dimensional elastic force (F_E), defined as the ratio of dimensional elastic force (F_e) and inertial force, is directly proportional to Young's modulus and thickness and inversely proportional to the diameter and base curve.

$$F_V = \left(\frac{\mu U_m L}{d}\right) * \left(\frac{L}{MU_m^2}\right) = \frac{\mu L^3}{MU_m d} = \frac{4\mu L^3}{\pi \rho_{cl} W_{cl}^2 H_{cl} U_m d} \tag{18}$$

$$F_E = F_e * \left(\frac{L}{MU_m^2}\right) = \frac{F_e L}{MU_m^2} = \frac{1}{3\pi}\left(\frac{L}{U_m^2}\right)\left(\frac{\varepsilon_m H_{cl}^2}{\rho_{cl}(1-\nu)W_{cl}}\right)\left[\frac{1}{R_{cl}} - \frac{1}{R_{sc}}\right]^2 \tag{19}$$

An area function is utilised to depict the area of a segment with a specified height from a circle, aligning with the methodology outlined by Chauhan and Radke (2001). Equation 20 gives the area of the CL covered by the lids, represented as an area function that defines the area of a segment of height (y) taken from a circle of radius (r).

$$\hat{A}(y, r) = r^2 \begin{cases} \frac{1}{2}\left[\text{acos}\left(2\left(1-\frac{y}{r}\right)^2 - 1\right) - 2\left(1-\frac{y}{r}\right)\sqrt{1-\left(1-\frac{y}{r}\right)^2}\right], & 0 < y \le r \\ \frac{1}{2}\left[2\pi - \text{acos}\left(2\left(1-\frac{y}{r}\right)^2 - 1\right) - 2\left(1-\frac{y}{r}\right)\sqrt{1-\left(1-\frac{y}{r}\right)^2}\right], & r < y \le 2r \end{cases} \tag{20}$$

This area function enables calculating the gap area between the CL and the eyelids and the area of the CL itself, as described in Eq. 21.

$$\begin{aligned} A_{cl} &= \pi\left(\frac{W_{cl}}{2}\right)^2 \\ A_{uplid}(t) &= \hat{A}\left(X(t) - X_{cl}(t) + \frac{W_{cl}}{2}, \frac{W_{cl}}{2}\right) \\ A_{lowlid}(t) &= \hat{A}\left(X_{cl}(t) + \frac{W_{cl}}{2} - 1, \frac{W_{cl}}{2}\right) \end{aligned} \tag{21}$$

Therefore, the equations of CL motion are detailed in Eq. 22.

$$\begin{aligned} \frac{dX_{cl}}{dt} &= U_{cl} \\ \frac{dU_{cl}}{dt} &= F_V\left[-\frac{A_{cl}}{D+\beta_{cl}+\beta_{eye}}U_{cl} + \frac{A_{uplid}(t)}{h_{lid}+\beta_{cl}+\beta_{lid}}\left(\frac{dX}{dt} - U_{cl}\right)\right. \\ &\quad \left. - \frac{A_{lowlid}(t)}{h_{lid}+\beta_{cl}+\beta_{lid}}U_{cl} + W_{cl}\int_X^1 \frac{U_s - U_{cl}}{h+\beta_{cl}}dx\right] - F_E sign(X_{cl}) \end{aligned} \tag{22}$$

where the initial conditions are defined as $X_{cl}(0) = 0$ and $U_{cl}(0) = 0$.

The resolution of the partial differential equations pertinent to these models is elaborately discussed in Anderson et al. (2021), which includes the numerical approach introduced in the previous literature (Braun and King-Smith 2007; Heryudono et al. 2007), where the moving domain ($X(t) \leq x \leq 1$) is converted to the fixed domain ($-1 \leq \xi \leq 1$). For computational implementation, the Chebyshev spectral method is employed for spatial discretisation (Kosloff and Tal-Ezer 1993; Trefethen 2000), complemented by the ode23s solver in MATLAB for temporal discretisation (Shampine and Reichelt 1997; The MathWorks Inc. 2021), facilitating the practical solution of these models. The forthcoming subsections will elaborate on the subject characteristics and material and geometric parameters pertinent to the CL.

2.2 Customizing Models with Subject Characteristics and Different CL Parameters

Adapting mathematical models to the unique ocular features of individuals is critical due to the variation in physiological factors like tear meniscus height, eyelid distance, and scleral curvature. The effectiveness of these models in reflecting the tear film behaviour of each subject relies on precise, subject-specific data. Consequently, there is a growing reliance on non-invasive diagnostic techniques that offer detailed insights into eye anatomy and function without causing patient discomfort. Utilising data from these advanced diagnostic tools enables the refinement of mathematical models, enhancing their ability to accurately represent the distinct tear film dynamics of individuals.

In this study, the parameters and outcomes are customised for a single subject, with ethical approval from the Ethics Committee of the Complutense University of Madrid. Table 1 presents the parameters indicative of tear film dynamics and specific subject characteristics for the single subject mentioned, obtainable via diverse laboratory instruments or imaging modalities. Parameters in bold emphasise traits unique

Table 1 Parameter values for tear film dynamics with blinking, highlighting subject-specific characteristics in bold, including variables like viscosity and surface tension reflective of individual eye health

Parameters	Values	Parameters	Values
Half-height palpebral fissure (L)	**5.5 mm**	**Initial tear meniscus height (h_0)**	**206 μm**
Characteristic tear film thickness (d)	5 μm	**Non-dimensional Initial tear volume (V_0)**	**8**
Length scale ratio ($\epsilon = d/L$)	9.1×10^{-4}	**Sclera radius of curvature (R_{sc})**	**12.2 mm**
Maximum blink closing speed (U_m)	**108 mm/s**	Gravitational acceleration (g)	9.81 m/s^2
Time scale (L/U_m)	0.051 s	Surface tension (σ_0) (Tiffany et al. 1989)	0.045 N/m
One blink cycle duration*	**0.32 s**	Viscosity (μ) (Tiffany 1991)	6 mPa s
PoLTF thickness (D)	2 μm	Density (ρ)	10^3 kg/m^3

*Blink period calculated from blinking characterisation as described in Fig. 4

to the subject, reflecting personal variability. For example, the palpebral fissure height ($2L$) is measured with a flexible ruler and Optical Coherence Tomography is employed to determine the tear meniscus height (h_0) (Raj 2016), while the scleral radius of curvature (R_{sc}) is assessed using a Pentacam (Upadhyaya et al. 2020). These parameters, alongside tear film properties such as viscosity and surface tension (Tiffany et al. 1989; Tiffany 1991), are critical as they fluctuate with the eye health of an individual. The current study focuses on a subject deemed to have healthy eyes, and thus, the viscosity and surface tension values listed are representative of a subject with healthy ocular conditions.

In the intricate interplay between CL wear and tear film dynamics, especially during the blinking process, the geometric and material properties of the CL emerge as critical factors. A comprehensive understanding of these parameters is essential for optimising CL design, aiming to enhance user comfort while maintaining effective tear film stability and distribution. In the context of CL design, understanding the forces at play between the CL and the tear film is paramount. The diameter of the CL is a critical parameter, especially when considering viscous forces, as outlined in the previous section. Furthermore, the elastic centring force, vital for maintaining the optimal position of the lens, is influenced by the base curve of the CL. This force is crucial for the alignment of the CL and depends on a range of factors, including the material properties of the lens, such as Young's modulus and Poisson's ratio, alongside its thickness, diameter, and base curve. These interactions underscore the importance of each geometric and material property in the design of the CL, affecting not only the comfort of the CL wearer but also the functional performance of the lens in synchrony with the dynamic tear film during eye movements.

This study does a comprehensive evaluation of the factors influencing tear film dynamics with CL interaction, which is undertaken through sixteen distinct simulations. Each simulation is meticulously designed to represent a unique CL configuration, with the specific details of these configurations enumerated in Table 2. To maintain consistency across the simulations, Poisson's ratio (ν) and the CL density (ρ_{cl}) were assumed to be constant, with the former set at 0.49 and the latter at 1500 kg/m^3. Additionally, the sclera radius of curvature and other tear film parameters, customised for an individual subject, are detailed in Table 1.

A plethora of methodologies, encompassing advanced imaging technologies and biomechanical assessments, enable the precise measurement of upper eyelid movement, shedding light on its dynamic function and implications for ocular health (Mas et al. 2010; Perez et al. 2011; Kwon et al. 2013; Lee et al. 2017; Espinosa et al. 2018). Among these, the Particle Image Velocimetry (PIVlab) application on MATLAB stands out for its accuracy in quantifying the nuanced motions of the eyelid (Thielicke and Stamhuis 2014; The MathWorks Inc. 2021). Digital particle image velocimetry (DPIV) is a non-intrusive method widely employed for quantitative flow mapping and particle tracking. The accuracy of DPIV flow measurements hinges on several computational steps, such as image pre-processing, sub-pixel peak estimation, data validation, interpolation, and smoothing techniques. PIVlab, an open-source tool for DPIV analysis, is available as a MATLAB toolbox (William Thielicke 2021a, b), featuring an intuitive graphical interface. This tool facilitates the calculation of velocity distributions at specific points within image pairs.

Table 2 Material and geometric parameters of different CLs (Kim et al. 2018)

No	CL brand	Young's modulus ϵ_m (MPa)	CL base curve R_{cl} (mm)	CL diameter W_{cl} (mm)	CL thickness H_{cl} (μm)
CL1	AirOptix Night & Day Aqua	1.44	8.6	13.8	80
CL2	Dailies	1.01	8.7	14	100
CL3	AirOptix Aqua	0.94	8.6	14.2	80
CL4	BioInfinity	0.8	8.6	14	80
CL5	Acuvue Oasys	0.74	8.8	14.3	70
CL6	Dailies Total 1	0.66	8.5	14.1	170
CL7	Biotrue	0.59	8.6	14.2	100
CL8	Clariti	0.56	8.6	14.1	175
CL9	Avaira	0.55	8.5	14.2	60
CL10	MyDay	0.53	8.4	14.2	80
CL11	Clariti 1Day	0.5	8.6	14.1	70
CL12	Proclear	0.49	8.6	14.4	90
CL13	Xtensa RX	0.47	8.7	14.4	100
CL14	Acuvue 2	0.45	8.3	14	84
CL15	Soflens	0.4	8.6	14.2	140
CL16	Acuvue Moist 1 Day	0.38	8.5	14.3	84

In this study, the velocity of the upper eyelid is determined using the PIVlab software to characterise blinking dynamics and obtain both the blink period and the peak velocity of the upper eyelid. These values are essential for modelling how the tear film behaves in the movement of CLs. The methodology involved both experimental and simulation steps. The experimental setup consisted of a custom-built table with a headrest to stabilise the head movement, allowing isolation of eyelid motion. For this study, a Sony Cyber-shot DSC-RX100 IV camera is employed, featuring a 20.1 MP 1″-type stacked CMOS sensor, an F1.8–2.8 24–70 mm equivalent Zeiss Vario-Sonnar T* lens, a maximum shutter speed of 1/32000 s, an ISO range of 125–12800, and a video resolution of 1920 × 1080. This camera is mounted on a tripod stand and captures at 500 frames per second (Perez et al. 2011; Kwon et al. 2013; Lee et al. 2017) and is used to record natural blinking. Recorded videos were then processed on a computer for further analysis. Pre-processing steps included converting video frames into individual red, green, and blue (RGB) channels and subsequently to grayscale images for simplicity (Saravanan 2010). This grayscale image will undergo principal component analysis to reduce noise in the frames.

The motion detection in PIVlab application is highly sensitive to image noise, which can lead to spurious results. To mitigate this, principal component decomposition is applied to filter the images. This technique generates principal components, which are linear combinations of the original images with zero correlation between them

and progressively decreasing variance values. Principal component decomposition is commonly used to reduce data dimensionality (López-Alonso et al. 2002; Lo´pez-Alonso 2002; Ng 2017). The coefficients for these linear combinations are derived from the eigenvectors of the covariance matrix of the data. The mathematical representation of this process is provided in Eq. 23.

$$Y_\alpha(p) = \sum_{t=1}^{N} e_\alpha(t)\left(F_t(p) - \overline{F_t}\right) \leftrightarrow F_t(p) - \overline{F_t} = \sum_{\alpha=1}^{N} e_\alpha(t) Y_\alpha(p) \tag{23}$$

where $Y_\alpha(p)$ is the α principal component at pixel "p", $F_t(p)$ is the image at time "t" and pixel "p", $\overline{F_t}$ is the mean value (over pixels) of image at time "t". $e_\alpha(t)$ are the eigenvectors of the covariance matrix S between images, as described in Eq. 24.

$$Se_\alpha = \lambda_\alpha e_\alpha \tag{24}$$

where λ_α is the eigenvalue associated with the eigenvector e_α.The eigenvalue associated with the eigenvector is used to measure the percentage of total data variance represented by each principal component α, as given in Eq. 25. This quantity, expressed as the ratio of the eigenvalue to the sum of all eigenvalues, provides insight into the significance of each component.

$$\Omega_\alpha = 100 * \frac{\lambda_\alpha}{\sum_\alpha \lambda_\alpha} \tag{25}$$

Using this method, the original images can be reconstructed with only the most representative principal components, discarding those primarily associated with noise. Various methods in the literature have been proposed to determine the optimal number of principal components, including approaches based on randomness tests, the differentiation of eigenvalues, or the identification of knee points in the eigenvalue curve as shown in Fig. 2 (scree plot). In this study, using the first fifteen principal components obtained from the randomness tests, account for 99.27% of the total variance. Figure 2 illustrates the percentage of total data variance versus the number of principal components, accompanied by examples of original and filtered images reconstructed using this approach for comparison. This preprocessing method significantly enhances the accuracy of the results obtained from PIVlab and will be utilized in subsequent analyses of blink speed.

In PIVlab, the region of interest is defined around the eyelid area. A Fourier transform window deformation algorithm, known for its accuracy in analysing complex image movements, is applied. This method used multiple passes, with an initial interrogation area of 64 pixels followed by 32 pixels with a 50% overlap in step size. After completing the PIV analysis, velocity maps were generated, displaying velocity vectors representing the magnitude and direction of eyelid movement. The PIV analysis are illustrated in Fig. 3, representing three phases of the blink cycle: (A) upstroke; (B) eye fully open and (C) downstroke phases of the blink cycle. Calibration of the data to physical dimensions is achieved by measuring the distance between the upper and

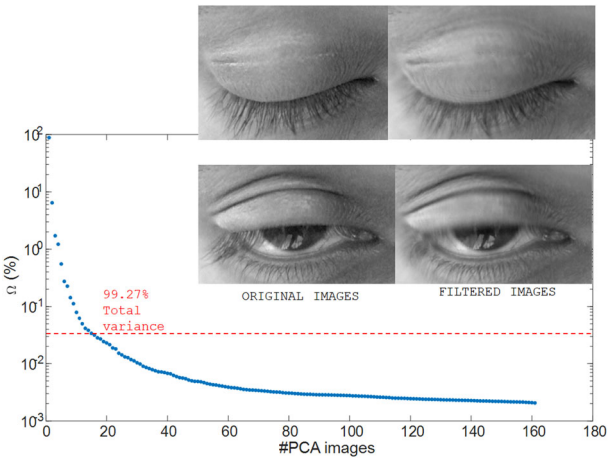

Fig. 2 Logarithmic percentage of variance versus number of PCA components. The first 15 components are used for image reconstruction, comprising 99.27% of total images variances. Two different original and filtered images are shown for comparison purposes

Fig. 3 PIV analysis at different phases of the blink cycle. **A** Upstroke phase, **B** Eye fully open, **C** Downstroke phase of the blink cycle

lower eyelids when the eye is open, using a flexible ruler that recorded this distance as 11 mm for the subject. Additional post-processing steps filtered out low-contrast and overly bright objects, ensuring high-quality data for analysis.

A custom MATLAB code then processes the PIVlab results, focusing on the x and y velocity components provided in m/s (Antonio Morales Sanjuán and José Manuel López-Alonso 2021). Since the upper eyelid movement is primarily vertical, the y-component of the velocity is selected as the main parameter for analysis. A detailed

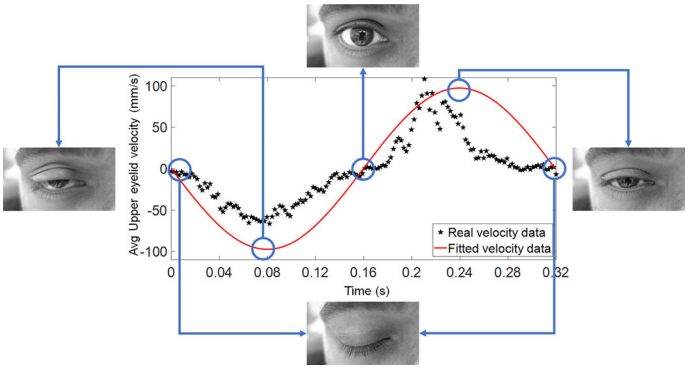

Fig. 4 Average (avg) upper eyelid velocity (mm/s) versus time (s). Blinking characterisation of the vertical velocity components that measures the period of the blink (ω_{blink}), which is equal to the time taken for one blink cycle, calculated from the maximum and minimum velocities of the upper eyelid observed at t = 0.08 s and t = 0.24 s, respectively ($\omega_{blink} = 2 \times (0.24—0.08) = 0.32$ s)

examination of each point in the PIVlab data indicated that the central region of the eye exhibited the highest velocity, which aligned closely with previous literature findings. The average y-velocity component of the upper eyelid is then calculated by averaging the values from the central region across each frame, focusing specifically on points covering the upper eyelid area. This computed y-velocity is compared with a sinusoidal function (Braun and King-Smith 2007), as shown in Fig. 4, to characterise the periodic movement of the upper eyelid during blinking. The blink period is calculated based on the maximum and minimum velocities of the upper eyelid, observed at times t = 0.08 s and t = 0.24 s, respectively. This results in a blink period of 2 × (0.24—0.08) = 0.32 s. Additionally, the maximum absolute velocity of the upper eyelid is recorded as 108 mm/s at time t = 0.24 s, which is updated in Table 1.

2.3 Descriptive Statistics and Data Distribution of PLTF Dynamics

Following the measurement of PLTF thickness for an individual subject using various CL types, this section of the study focuses on analysing descriptive statistics related to PLTF thickness. Employing a linear correlation methodology, the research investigates the influence of diverse CL parameters on PLTF dynamics. It provides a detailed examination of CL properties such as Young's modulus, base curve, diameter, and thickness, as detailed in Table 2. By conducting a thorough cross-analysis of these parameters against critical PLTF metrics, the study aims to determine how alterations in CL design impact the behaviour and distribution of the tear film across the ocular surface. This approach clarifies the relationship between the physical properties of CLs and tear film stability, contributing to a deeper understanding of their interaction and effects on ocular health.

In the initial phase of this study, a detailed analysis of PLTF thickness was performed using kernel distribution, a nonparametric method for constructing probability density functions (PDFs) for each CL type (Bowman and Azzalini 1999; The MathWorks Inc.

2023a, b). For this study, the PDFs were generated in MATLAB using the "ksdensity" function (The MathWorks Inc. 2023b), with the normal (gaussian) kernel serving as the default smoothing function. The kernel density estimator, which defines the estimated PDF of a random variable, is described in Eq. 26. In this equation, for any real values of x, x_i represents the random samples drawn from an unknown distribution, n denotes the sample size, $K(.)$ stands for the kernel or smoothing function, and b is the bandwidth parameter that determines the smoothness of the estimator ($\widehat{f_b}(x)$). This statistical approach enabled the identification of PLTF thickness values showing significant differences across various CL types. Through detailed examination of these PDFs, specific ranges of PLTF thickness where the most substantial variations were observed were pinpointed.

$$\widehat{f_b}(x) = \frac{1}{nb} \sum_{i=1}^{n} K\left(\frac{x - x_i}{b}\right) \tag{26}$$

To verify the PDFs (Parzen 1962), they must satisfy specific conditions, as outlined in Eq. 27.

$$\begin{aligned} &\widehat{f_b}(x) \geq 0, \quad for\ all\ x \in \mathbb{R} \\ &\int_{-\infty}^{\infty} \widehat{f_b}(x)dx = 1 \end{aligned} \tag{27}$$

The PDFs must be verified to ensure they correctly represent probability distributions. This verification confirms that PDFs are non-negative and integrated to one, guaranteeing the validity of statistical models. Accurate PDFs are crucial for hypothesis testing, simulation accuracy, and reliable statistical analysis, ensuring that conclusions drawn from data are based on sound probabilistic foundations.

The PDFs for PLTF thickness enable the identification of specific regions where PLTF thickness is of interest. These regions are selected based on the corresponding PDFs, which exhibit a Gaussian-like distribution, particularly emphasizing central areas of interest. Once the critical PLTF thickness values were identified from the PDFs, descriptive statistics were applied to these targeted measurements for each CL type, as summarized in Table 2. The formulas for calculating the descriptive statistics of variable X— where $\overline{X}$ and σ_X represent the mean and standard deviation of X, both expressed in μm, and s and k denote the skewness, and kurtosis of X, which are dimensionless—are presented in Eq. 28.

$$\begin{aligned}
\overline{X} &= \frac{1}{n}\sum_{i=1}^{n} X_i \\
\sigma_X &= \sqrt{\frac{1}{n-1}\sum_{i=1}^{n}\left|X_i - \overline{X}\right|} \\
s &= \frac{\frac{1}{n}\sum_{i=1}^{n}\left(X_i - \overline{X}\right)^3}{\left(\sqrt{\frac{1}{n}\sum_{i=1}^{n}\left(X_i - \overline{X}\right)^2}\right)^3} \\
k &= \frac{\frac{1}{n}\sum_{i=1}^{n}\left(X_i - \overline{X}\right)^4}{\left(\sqrt{\frac{1}{n}\sum_{i=1}^{n}\left(X_i - \overline{X}\right)^2}\right)^4}
\end{aligned} \tag{28}$$

Building on this groundwork, Pearson correlation analysis is employed to delve deeper into the relationship between various CL parameters and tear film behaviour (Schober et al. 2018). Pearson correlation, a widely used method for assessing linear relationships, evaluates the strength and direction of associations between two variables through the correlation coefficient (r) and p value (p). Equation 29 defines the correlation coefficient as the quotient of the covariance of two variables and the product of their respective standard deviations (The MathWorks Inc. 2023c), which can span from -1 to 1. A positive correlation (r between 0 and 1) indicates that variables change in the same direction, and a negative correlation (r between -1 and 0) suggests they move in opposite directions. A correlation coefficient value of 0 indicates no correlation. Correlations with a p-value less than 0.05 are considered statistically significant, highlighting meaningful relationships that warrant further investigation to enhance CL design and improve ocular health outcomes.

$$r = \frac{\sum_{i=1}^{n}\left(X_i - \overline{X}\right)\left(Y_i - \overline{Y}\right)}{\sum_{i=1}^{n}\left(X_i - \overline{X}\right)^2 \sum_{i=1}^{n}\left(Y_i - \overline{Y}\right)^2} \tag{29}$$

where X_i and Y_i represent the individual data points for variables X and Y respectively, $\overline{X}$ and $\overline{Y}$ denote the mean values of the X and Y datasets, respectively (The MathWorks Inc. 2023c).

In the analytical framework, the mean tear film thickness gauges the overall thickness of the tear film, while the standard deviation provides insights into its stability and uniformity. Additionally, skewness and kurtosis examine the asymmetry and presence of anomalous values, respectively. This section culminates in calculating Pearson correlation coefficients, with 95% confidence intervals, for these descriptive statistics against the lens parameters used in the simulation. The upcoming section presents results from computational models incorporating subject characteristics and various CL parameters, detailed in Tables 1 and 2, developed using MATLAB software (The MathWorks Inc. 2021). It includes analyses based on PDFs that outline data distribution and execute a descriptive examination of PLTF thickness. Leveraging Pearson

correlation, it decodes which CL parameters significantly impact PLTF thickness, further elucidating the nature and magnitude of these relationships.

3 Results

This section is dedicated to exploring the influence of CL parameters on the PLTF dynamics to enhance the understanding of their significance in CL wear. The PLTF thickness emerges as a critical factor in this context, with substantial implications for the comfort and functionality of CL usage, as well as for overall ocular health and lens efficacy. Figure 5 illustrates the PLTF thickness throughout one complete blink cycle, modelled using sinusoidal eyelid motion to replicate full blinks. The figure is organised into three columns highlighting various aspects of the blink cycle. The

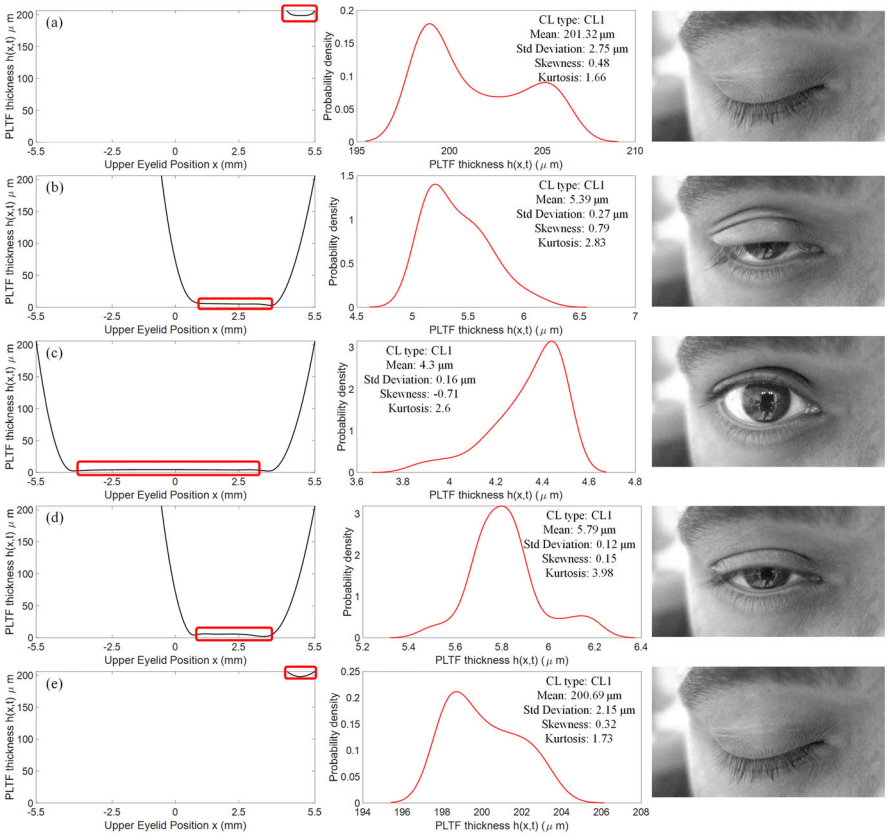

Fig. 5 PLTF thickness for one blink cycle using sinusoidal lid motion for full blinks of the CL1 type. Left column: PLTF thickness versus Upper eyelid position at distinct phases of blink cycle; middle column: PDFs with its respective descriptive statistics; right column: real eye movement. **a** Eye closed, **b** Opening of the eye (upstroke), **c** Eye fully open, **d** Closing of the eye (downstroke), **e** Eye closed again

left column relates the PLTF thickness with the upper eyelid position at various blink phases, providing a dynamic view of the variability of the tear film. The middle column presents a PDFs, offering a statistical analysis of PLTF thickness distributions during the blink. The right column captures actual eye movements, grounding the predictions in the real-life physiological behaviour of the model. The sequence includes five stages: (a) the eye fully closed, (b) the opening phase or upstroke, (c) the eye at maximum openness, (d) the closing phase or downstroke, and (e) the eye closed again, effectively mapping the cyclical nature of eyelid movement and its impact on tear film thickness.

In this study, PDFs for PLTF thickness have been elucidated, centring on values that typify the tear film across various phases, barring the closed-eye state. During eye closure, the PDFs exhibit a bimodal distribution with two distinct peaks, as presented in Fig. 5a, e, signifying two dominant PLTF thickness measurements within the evaluated population or given condition. Consequently, the closed-eye phase is considered negligible for this purpose due to consistent PDFs across different CL types. Conversely, the upstroke phase, portrayed in Fig. 5b, shows PDF concentration around a PLTF thickness near 5.4 μm, signifying a central tendency of data points. Open-eye and downstroke phases, depicted in Fig. 5c, d, similarly demonstrate a clustering of PLTF thickness around their respective mean values. This pattern underscores a uniform distribution of PLTF thickness throughout the various phases of the blink cycle, shedding light on the dynamic behaviour of the tear film.

Following the initial analysis of PDFs for PLTF thickness across various phases of the blink cycle, as illustrated in Fig. 5, the PDFs in this study were essential for isolating specific regions within the overall distribution of PLTF thickness values. This method enabled a targeted analysis of subdomains where the variation in PLTF-related parameters—such as diameter, thickness, base curve, and Young's modulus—is limited, facilitating a more precise understanding of their impact on PLTF dynamics. By isolating segments of the PLTF thickness distribution, particularly areas where thickness values are densely clustered or exhibit extreme values, the analysis sheds light on how these CL characteristics influence tear film stability, uniformity, and variability. This targeted use of PDFs enables the detection of subtle trends that may be obscured in a broader analysis, making it a valuable approach for examining the interaction between CL parameters and tear film dynamics.

Five PDFs were created for each simulation to represent different CL brands, resulting in a total of 80 PDFs, each corresponding to a specific phase of the blink cycle. These phases include the eye closed at $t_{PDF} = 0$s, followed by upstroke $t^*_{PDF} = 0.08$s, eye fully open $t^*_{PDF} = 0.16$s, downstroke $t^*_{PDF} = 0.24$s, and concluding with the eye closed again after blinking $t^*_{PDF} = 0.32$s. For each of these times, t^*_{PDF}, the PDFs are constructed using the values of $h(x, t^*_{PDF})$, representing the spatial locations along the vertical axis of the eye, as indicated in Fig. 5. Here, $x^* = 0$ corresponds to the center of the eye, extending across the total eye height from -5.5 to 5.5 mm, which is the distance between the lower and upper eyelids (given as 11 mm in Table 1 of the revised manuscript). The exact values for these regions are detailed in Table 3.

The default Gaussian kernel smooths data across the range to produce a density estimate that balances bias and variance, using an automatic bandwidth selection rule to optimize the kernel window. For instance, when the eye is fully closed ($t^*_{PDF} = 0$),

Table 3 Spatial regions (x^* in mm) used for constructing PDFs during each phase of the blink cycle for each simulation. The x-values range from −5.5 to 5.5 mm with $x = 0$ represent the centre of the eye

t^*_{PDF}(s)	Blink cycle phase	Spatial domain (x^* in mm)
0	Eye closed at the beginning of time	(4.4, 5.5)
0.08	Upstroke	(0.96, 3.3)
0.16	Eye fully open	(-3.2, 2)
0.24	Downstroke	(1.1, 2.48)
0.32	Eye closed after blinking	(4.4, 5.5)

with $b = 1.0188$ across all simulations due to identical initial conditions. During the upstroke phase, b is between 0.1408 and 0.1468; in the fully open-eye phase, b is between 0.0622 and 0.0634; in the downstroke phase, b is between 0.0524 and 0.0598; and finally, when the eye closes again after blinking, b between 1.5388 and 1.5425.

Additionally, the integral of $\widehat{\mathrm{f_b}}(\mathrm{x})$ for the fully closed-eye phase at the beginning of the cycle ($t^*_{PDF} = 0$s) is approximately 0.9996 across all 16 simulations. At the end of the blink cycle, when the eye is closed again, the integral value is around 0.9997 for all simulations with various CL types. During the upstroke phase, the integral is 0.9999, while in the open-eye and downstroke phases, it is 0.9998. These values remained consistent across all simulations for each phase, confirming that the integral of $\widehat{\mathrm{f_b}}(\mathrm{x})$ is nearly one. Such minor deviations (e.g., 0.999) are typical in kernel density estimation, indicating that the PDFs are effectively normalized. These slight discrepancies are expected in numerical computations with real-world data and are generally acceptable in statistical analyses.

The targeted measurements of the PLTF thickness, as highlighted by the red boxes in the PLTF thickness vs. upper eyelid position plots in Fig. 5, are selected based on the corresponding PDFs. The PDFs determined for the PLTF thickness exhibit an approximately Gaussian distribution, as shown in the plots, particularly in the central regions of interest. This observation is consistent across the different cases. Proceeding from the analysis of the PDFs for PLTF thickness, the study transitions to a comparative examination of the targeted PLTF thickness against various CL parameters specified in Table 2. This comparison utilises the correlation coefficient (r) and p value (p), alongside the lower (r_l) and upper (r_u) bounds of the correlation coefficient, to delineate the extent and nature of linear relationships. These bounds are critical in elucidating the scope of the correlation, thereby offering a precise and interpretable metric for analysing how distinct CL parameters affect the PLTF thickness. This comprehensive statistical approach aids in discerning the impact of varying CL designs on the distribution and dynamics of the tear film, contributing to the optimisation of lens performance and wearer comfort.

Subsequent subsections explore the impact of various CL parameters on critical tear film metrics, providing an in-depth analysis of their effects on tear film behaviour throughout distinct phases of the blink cycle. The primary focus will be on the three pivotal phases of the blink cycle: the upstroke, the fully open-eye phase, and the downstroke.

3.1 Influence of CL Diameter

In this section of the study, the interplay between CL diameter and PLTF dynamics is investigated. Utilising data presented in Table 4, this analysis spans the entire blink cycle, divided into three distinct phases, to delineate the relationship between the diameter of the CLs and the tear film behaviour across these phases.

During the upstroke phase of the blink cycle, there is a significant negative correlation between the CL diameter and the mean tear film thickness, with larger CL diameters corresponding to thinner tear films. Concurrently, the standard deviation of tear film thickness shows a positive correlation with CL diameter, indicating a trend towards increased variability with larger lenses, which may impact the ocular health of CL users. Despite these changes, the skewness of the distribution exhibits a substantial negative correlation yet demonstrates minimal variance with different CL diameters, indicating a stable asymmetry in the distribution of tear film thickness regardless of CL diameter. Furthermore, kurtosis is revealed to have a negligible and statistically insignificant correlation, denoting that the peakedness of the tear film thickness distribution remains unaffected amidst variations in CL diameter throughout the upstroke phase.

Further analysis during the fully open eye phase showed strong positive correlations between the CL diameter and the mean thickness, standard deviation, and skewness of the PLTF. This highlights a pronounced and statistically significant relationship, demonstrating that increased CL diameter is associated with increases in PLTF thickness, variability, and asymmetry. Consequently, a larger CL diameter is indicative of a thicker tear film, which could infer a reduced impact on wearer comfort and ocular health. In contrast, kurtosis revealed a significant negative correlation, implying that larger CL diameters tend to produce a distribution with less pronounced tails, denoting reduced peakedness. The trends observed in skewness and kurtosis—toward slightly improved symmetry and decreased likelihood of extreme values in tear film thickness, respectively—suggest a progression toward a more normal distribution of PLTF thickness as CL diameter enlarges.

In the downstroke phase of the blink cycle, analysis revealed a persistent negative correlation between the CL diameter and the mean tear film thickness, thereby corroborating the trend of the upstroke of the blink cycle that larger CL diameters are associated with a reduction in tear film thickness. Simultaneously, a positive correlation between CL diameter and the standard deviation is observed, indicating that the variability of tear film thickness tends to increase with larger CL sizes. These findings suggest that as CL diameter enlarges, the tear film not only thins but also exhibits greater dispersion. Moreover, a positive trend in both skewness and kurtosis were identified, which points to a progressive shift towards a more asymmetrical and leptokurtic distribution, suggesting an enhanced occurrence of both exceptionally thin and thick tear film measurements in conjunction with increasing CL diameter.

These observations highlight the crucial role of CL diameter in tear film dynamics and CL design, as evidenced by the reliability and significance outlined in Table 4. This underscores its importance in CL design and fitting throughout the blinking cycle.

Table 4 Correlation analysis between CL diameter and key PLTF metrics, presented with 95% confidence intervals. Metrics include the correlation coefficient (r), lower bound (r_l), upper bound (r_u), and the *p* value (*p*)

Tear film parameters/Correlation coefficient	Upstroke			Eye fully open			Downstroke		
	r		*p*	r		p	r		*p*
	r_l	r_u		r_l	r_u		r_l	r_u	
Mean	−0.985		$4.54e^{-12}$	0.996		$4.34e^{-16}$	−0.744		0.001
	−0.995	−0.956		0.988	0.999		−0.906	−0.393	
Standard deviation	0.996		$1.93e^{-16}$	0.986		$2.34e^{-12}$	0.947		$2.63e^{-8}$
	0.989	0.999		0.960	0.995		0.851	0.982	
Skewness	−0.885		$5.38e^{-6}$	0.991		$1.19e^{-13}$	0.979		$5.43e^{-11}$
	−0.960	−0.692		0.974	0.997		0.938	0.993	
Kurtosis	−0.213		0.429*	−0.994		$8.89e^{-5}$	0.981		$2.33e^{-11}$
	−0.641	0.316		−0.998	−0.982		0.945	0.994	

*Represents no statistically significant correlation

3.2 Influence of Young's Modulus

The study commenced with an evaluation of the influence exerted by Young's Modulus on tear film dynamics, uncovering a significant association with tear film behaviour. Table 5 summarises the results of the correlation analysis, providing quantitative measures of the strength and statistical significance of the relationship.

In the upstroke phase of the blink cycle, a statistically significant moderate positive correlation is observed between Young's modulus and the mean tear film thickness, indicating that an increase in material stiffness might lead to a thicker tear film on average. Conversely, the standard deviation showed a moderate negative correlation, also significant, suggesting that a stiffer CL material could result in more uniform tear film thickness. Skewness exhibited a weaker yet significant positive relationship, hinting at a longer tail in the tear film thickness distribution as the Young's modulus increases. Kurtosis, however, is negligibly correlated and not statistically significant, indicating that the extremity of the tails of the data distribution is unaffected by changes in the stiffness of the CL material.

Following the observed trends during the upstroke phase of the blink cycle, the study further reveals contrasting patterns when the eye is fully open. The correlation analysis indicates a moderate negative relationship between Young's modulus and the mean tear film thickness during this phase, suggesting a thinner tear film is associated with increased material stiffness, a notable shift from the upstroke phase. Similarly, the standard deviation of the tear film thickness during the open-eye phase mirrors this trend, where increased stiffness correlates with reduced variability, hinting at the possibility of a more homogenous tear film with stiffer materials. Skewness continues to demonstrate a negative correlation, pointing to a distribution with a longer left tail as the Young's modulus increases, a contrast to the positive skewness seen in the upstroke phase. Furthermore, in terms of kurtosis, the open-eye phase shows significant change, which implies that the tails of the data distribution become heavier as Young's modulus increases, suggesting a more peaked distribution with more extreme values in tear film thickness as the material stiffness increases.

During the downstroke phase of the blink cycle, there is a positive correlation between Young's modulus and the mean tear film thickness, indicating that materials with greater stiffness are associated with an increase in mean tear film thickness. Conversely, standard deviation and measures of distribution shape, skewness, and kurtosis, all show negative correlations with Young's modulus. This reveals that as the stiffness of the CL material increases, there is a tendency toward reduced variability in tear film thickness, with distributions exhibiting less skewness and flatter tails. These findings suggest that the mechanical properties encapsulated by Young's modulus can significantly influence the stability and uniformity of the tear film over the course of a blink.

These observations emphasise Young's modulus's influence on tear film dynamics and CL design, confirmed by the bounds of the correlation coefficient in Table 5. Although statistically significant, Young's modulus affects tear film dynamics less than CL diameter, positioning it as the second most critical factor in CL design.

Table 5 Correlation analysis between Young's modulus and key PLTF metrics, presented with 95% confidence intervals. Metrics include the correlation coefficient (r), lower bound (r_l), upper bound (r_u), and the *p* value (*p*)

Tear film parameters/Correlation coefficient	Upstroke			Eye fully open			Downstroke		
	r		*p*	r		*p*	r		*p*
	r_l	r_u		r_l	r_u		r_l	r_u	
Mean	0.643		0.007	−0.641		0.008	0.512		0.043
	0.216	0.863		−0.863	−0.213		0.022	0.804	
Standard deviation	−0.654		0.006	−0.619		0.011	−0.538		0.032
	−0.868	−0.234		−0.853	−0.177		−0.816	−0.058	
Skewness	0.469		0.067*	−0.653		0.006	−0.680		0.004
	−0.034	0.783		−0.868	−0.233		−0.879	−0.278	
Kurtosis	0.011		0.969*	0.664		0.005	−0.616		0.011
	−0.488	0.504		0.251	0.873		−0.852	−0.173	

*Represents no statistically significant correlation

3.3 Influence of Base Curve

This section delves into the base curve of CLs and its effect on PLTF dynamics. Utilising Table 6, the analysis delineates the relationship between the CL base curve and PLTF thickness throughout the three distinct phases of the blink cycle. It reveals that during the upstroke, the base curve shows a negligible relationship with tear film thickness, as evidenced by weak and statistically insignificant correlations across mean thickness, standard deviation, skewness, and kurtosis. This trend persists when the eye is fully open; the influence of the base curve on PLTF metrics is statistically insignificant, with only slight positive correlations noted for mean thickness, standard deviation, and skewness, and a small negative correlation for kurtosis, implying the dominance of other factors over the base curve in affecting tear film properties. Similarly, in the downstroke phase, the impact of the base curve on tear film thickness remains limited, supported by weak correlations that lack statistical significance. The bounds of the correlation coefficients, being opposite to each other, further reinforce the minimal influence of base curve on PLTF dynamics. Collectively, these findings across all blink cycle phases suggest that the role of the base curve in modulating tear film thickness and its variability is overshadowed by other variables that more profoundly affect tear film dynamics.

3.4 Influence of CL Thickness

The study examines the influence of CL thickness on PLTF dynamics and finds that across the blink cycle phases—upstroke, fully open eye, and downstroke—there are only marginal negative correlations between CL thickness and mean PLTF thickness, but these correlations are not statistically significant as outlined in Table 7. The analysis further shows very weak correlations between CL thickness and PLTF metrics such as standard deviation, skewness, and kurtosis, emphasising their minimal impact on the variability and distribution of tear film thickness. Overall, the negligible influence of CL thickness on these tear film parameters suggests that there are other, more impactful factors that dictate PLTF dynamics. The opposite bounds of the correlation coefficients further emphasise the minimal impact of CL thickness on tear film dynamics. These findings highlight the complex nature of the interactions that determine tear film behaviour, pointing to the need for a broader investigation into the variables that influence the tear film beyond just CL thickness.

4 Discussion

In this study, the mathematical models were employed to analyse tear fluid and tear film dynamics in conjunction with blinking and CL motion (Chauhan and Radke 2001; Anderson et al. 2021). The model incorporates subject-specific characteristics for a single subject, allowing for the personalisation of simulations to reflect individual variability in tear film behaviour. A focal point of the methodology is the examination of critical CL parameters—Young's modulus, base curve, diameter, and thickness—and

Table 6 Correlation analysis between CL base curve and key PLTF metrics, presented with 95% confidence intervals. Metrics include the correlation coefficient (r), lower bound (r_l), upper bound (r_u), and the *p* value (*p*)

Tear film parameters/Correlation coefficient	Upstroke			Eye fully open			Downstroke		
	r		*p*	r		*p*	r		*p*
	r_l	r_u		r_l	r_u		r_l	r_u	
Mean	−0.290		0.275*	0.221		0.411*	−0.347		0.188*
	−0.687	0.239		−0.309	0.646		−0.719	0.179	
Standard deviation	0.229		0.393*	0.249		0.353*	0.313		0.238*
	−0.301	0.651		−0.282	0.663		−0.217	0.699	
Skewness	−0.314		0.237*	0.255		0.341*	0.178		0.511*
	−0.701	0.216		−0.276	0.666		−0.349	0.619	
Kurtosis	−0.240		0.371*	−0.241		0.369*	0.263		0.326*
	−0.658	0.290		−0.658	0.289		−0.268	0.671	

*Represents no statistically significant correlation

Table 7 Correlation analysis between CL thickness and key PLTF metrics, presented with 95% confidence intervals. Metrics include the correlation coefficient (r), lower bound (r_l), upper bound (r_u), and the *p* value (*p*)

Tear film parameters/Correlation coefficient	Upstroke			Eye fully open			Downstroke		
	r		*p*	r		*p*	r		*p*
	r_l	r_u		r_l	r_u		r_l	r_u	
Mean	−0.048		0.861*	−0.062		0.820*	−0.266		0.319*
	−0.531	0.459		−0.541	0.448		−0.673	0.264	
Standard deviation	0.019		0.945*	−0.003		0.991*	−0.213		0.429*
	−0.509	0.482		−0.498	0.493		−0.641	0.316	
Skewness	−0.224		0.405*	0.032		0.908*	0.125		0.645*
	−0.306	0.647		−0.472	0.519		−0.395	0.584	
Kurtosis	−0.461		0.072*	−0.033		0.905*	−0.098		0.719*
	−0.045	0.779		−0.520	0.471		−0.566	0.482	

*Represents no statistically significant correlation

their influence on tear film dynamics. The influence of these parameters is studied through descriptive statistics, including mean, standard deviation, skewness, and kurtosis of tear film thickness, which describe the thickness, stability, asymmetry, and anomalies in the tear film. To achieve a comprehensive evaluation, sixteen distinct simulations were conducted, each corresponding to a different CL configuration, utilising a diverse array of sixteen CL brands (Kim et al. 2018). This method emphasises capturing the nuances of CL-tear film interaction and broadens the relevance of the findings across various CL types and wear scenarios. It lays a solid foundation for further analysis and discussion on the relationship between CL properties and tear film dynamics.

The mathematical model by Anderson et al. (2021) integrates key physiological processes, including eyelid motion, tear film dynamics, and dynamic models for CL movement (Chauhan and Radke 2001). Coupled with partial differential equations for tear film thickness, this approach enables an in-depth analysis of tear film behaviour over the CL in response to various blinking motions. By adapting boundary conditions to account for the CL presence and movement, the model provides a realistic and comprehensive representation compared to models that may overlook these factors. This adaptability makes the model a valuable tool for studying tear film dynamics and CL interactions.

However, the model has certain limitations. It does not account for the suction pressure generated along the PoLTF (Martin and Holden 1986; Maki and Ross 2014), which could affect findings related to parameters like the CL base curve. Additionally, the model relies on assumptions and simplifications, such as treating the CL as impermeable and rigid and assuming a fixed PoLTF thickness, which may not fully capture physiological variability across individuals or conditions. The model can currently be validated only by comparing its results with measurements reported in the literature, where most studies provide mean values of PLTF thickness measured using interferometry or optical coherence tomography. These mean values, typically ranging between 3 and 5 μm (Nichols and King-Smith 2003, 2004; Wang et al. 2003), serve as valuable metrics for validation. In most cases, mean PLTF thickness is measured when the eye is fully open, either immediately after a blink or 2 s later, allowing the tear film to redistribute and stabilize. The findings of this study align closely with these reported values, with mean PLTF thickness values of approximately 3–5 μm, as illustrated in Fig. 5. Addressing these limitations, especially by incorporating PoLTF dynamics and performing experimental validation, would enhance the accuracy and practical relevance of the model in predicting tear film and CL interactions.

The forces exerted by CLs, expressed in both dimensional and non-dimensional terms, are influenced by key CL properties, including thickness, diameter, base curve, Young's modulus, and Poisson's ratio (Chauhan and Radke 2001; Anderson et al. 2021). The dimensional elastic force (F_e) is directly proportional to the Young's modulus, thickness, and diameter of the CL, while inversely proportional to the base curve. In comparison, the non-dimensional elastic force (F_E) exhibits a similar dependence on Young's modulus and thickness but is inversely related to the diameter and base curve. Furthermore, the non-dimensional viscous force (F_V) is inversely proportional to both the CL diameter and thickness. These relationships illustrate the non-linear interactions between CL parameters and non-dimensional viscous and elastic forces,

emphasizing that these forces alone do not fully account for CL motion and PLTF dynamics. The integration of these forces into the equation governing CL motion (Eq. 22) demonstrates that CL behaviour is influenced by a combination of factors, including upper eyelid velocity, PLTF thickness, and other tear film parameters, highlighting the complexity of CL dynamics and their interactions with tear film properties. In this study, the main focus is on the three phases of the blink cycle, which occur at different moments in time: the upstroke phase at 0.08 s, the eye fully open phase at 0.16 s, and the downstroke phase at 0.24 s.

In this study, the interaction between CL parameters and tear film behaviour during various phases of the blink cycle is meticulously analysed, revealing that CL diameter significantly influences PLTF dynamics. During the upstroke phase, no statistically significant relationship is found between CL diameter and the kurtosis of tear film thickness, indicating that anomalies in tear film thickness cannot be reliably controlled by adjusting CL diameter. Correlation analysis identified CL diameter as a pivotal factor affecting tear film thickness, variability, and distribution, especially during the open-eye and downstroke phases. This highlights the critical role of CL diameter in design, with significant implications for wearer comfort and eye health, emphasizing the importance of considering diameter variations in tear film interactions.

The correlation between CL diameter and PLTF thickness exhibits distinct patterns: negative correlations are observed in the upstroke and downstroke phases where smaller CL diameters are associated with increased PLTF thickness, suggesting an inverse relationship. Conversely, a positive correlation emerges during the fully open-eye phase, with larger diameters correlating with thicker PLTF. For example, in the upstroke phase, while PLTF thickness generally remains consistent across different lens types, notable variations on the right side of Fig. 6A demonstrate that smaller diameters tend to increase PLTF thickness. This shift continues in the fully open-eye phase, where a decrease in CL diameter results in reduced PLTF thickness, indicating a direct relationship, as illustrated in Fig. 6B. Similarly, although PLTF thickness is relatively consistent during the downstroke phase, the right side of the plot in Fig. 6C shows smaller diameters correlating with thicker PLTF values, reinforcing the inverse correlation seen in the upstroke phase. These observations highlight the complex interaction between CL diameter and tear film dynamics, underscoring the significant impact of lens physical properties on tear film stability across different phases of the blink cycle.

The findings of this study expand on the current understanding of role of the CL diameter in PLTF dynamics, offering insights that are particularly relevant during the eye-open phase—a critical period for ocular surface hydration. This aligns with a body of research exploring the intricate relationship between various CL parameters and their implications for ocular health and the CL performance. Although direct references to PLTF thickness were not made (McNamara et al. 1999), the implications of tear mixing—integral for the maintenance of tear film homeostasis—were noted. Inadequate mixing could result in a stagnant and potentially thinner tear film over time for larger CL diameter, particularly if tear fluid evaporation surpasses the rate of replenishment. Complementing these findings, other studies, such as those examining the use of large-diameter multifocal CLs by presbyopic adults with dry eye syndrome (Hsiao et al. 2023), have shed light on the complex influence of CL diameter. These

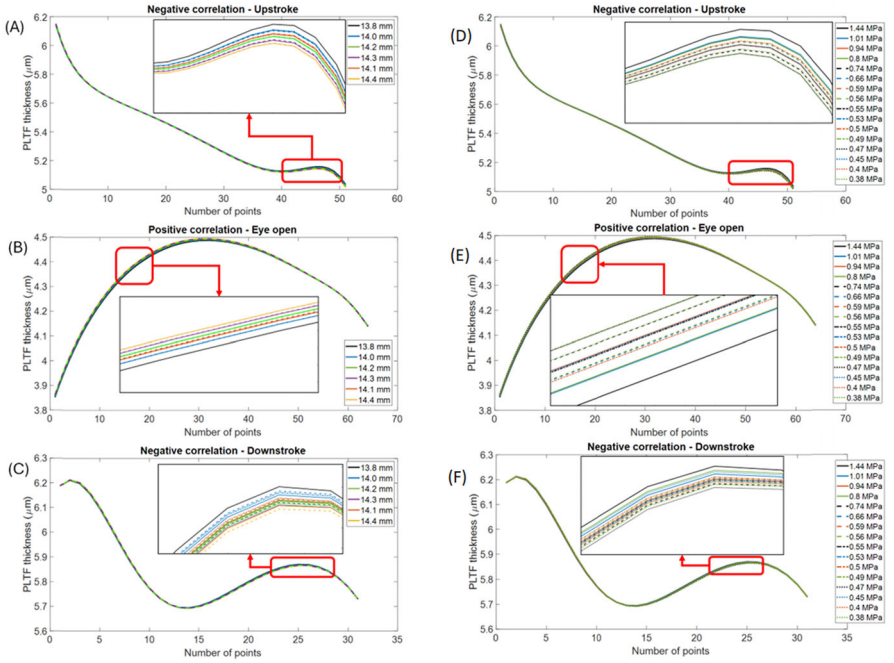

Fig. 6 **A**–**C** PLTF thickness values with respect to CL diameter obtained after the analysis of the PDF, focusing only on the clustered values. **D**–**F** PLTF thickness values with respect to CL Young's modulus were obtained after the analysis of the PDF, focusing only on the values clustered around the mean. **A**, **D** Upstroke, **B**, **E** Eye full open and **C**, **F** Downstroke phases of the blink cycle. In all the cases, the x-axis represents the number of points in the sample space derived from the PDFs

studies suggest that CL diameter has significant, multifaceted impacts on the ocular surface environment, visual acuity, and overall visual function.

The analysis also underscores the significant impact of material stiffness, as indicated by Young's modulus, on PLTF dynamics, identifying it as the second most influential parameter. The material stiffness variably affects PLTF thickness and distribution throughout the blink cycle. During the upstroke phase, there is no statistically significant relationship between Young's modulus and the skewness or kurtosis of tear film thickness, suggesting that stiffness does not systematically affect the asymmetry or extremes of the tear film thickness distribution. However, significant correlations during the open-eye and downstroke phases underscore the importance of material stiffness in maintaining tear film stability and homogeneity, as these phases show statistically significant correlations between Young's modulus and all PLTF metrics.

In examining the relationship between Young's modulus and PLTF thickness, positive correlation coefficients were observed during the upstroke and downstroke phases of the blink cycle, where higher values of Young's modulus correspond to increased PLTF thickness. Conversely, the highest values of Young's modulus are associated with reduced PLTF thickness, indicating a negative correlation. The response of PLTF thickness to changes in Young's modulus appears less consistent. However, the highest

values generally correspond to greater thickness, and values near the lowest modulus show reduced thickness in both phases. Figure 6D–F describes the PLTF thickness values concerning CL Young's modulus obtained after the PDF analysis, focusing only on the values clustered around the mean. These findings indicate that PLTF dynamics are influenced by a complex interplay of factors and not solely by Young's modulus.

Building on the findings of this study, related research has examined the impact of CL material, design, and fitting characteristics on user discomfort. Specifically, a study found that lenses exhibiting less movement are linked to improved comfort (Stapleton and Tan 2017). This aligns with the observations from the upstroke and downstroke phases of the blink cycle, where an increase in Young's modulus is correlated with an increase in PLTF thickness. The implication is that a thicker tear film, potentially resulting from a stiffer lens material, could enhance lubrication and reduce lens movement, thereby increasing wearer comfort. Additionally, another study on tear fluid exchange suggests that stiffer, thicker lenses may enhance PoLTF exchange due to larger mechanical suction pressure gradients (Maki and Ross 2014). This indicates that the mechanical properties of CLs, including Young's modulus, play a significant role in both tear film dynamics and user comfort.

Conversely, the study finds that the base curve and thickness of CLs have a comparatively minor impact on PLTF dynamics than Young's modulus and diameter. Research demonstrating how variations in base curve and thickness affect lens fit through mathematical modelling aligns with the observations, reinforcing that these parameters might not be the primary influencers of PLTF dynamics (FINK et al. 1992; Young et al. 2017). Further investigations into lens movement and oxygen uptake in relation to base curve changes corroborate the notion that while base curve adjustments can influence tear pump efficiency, their overall effect on tear film is constrained (Muntz et al. 2015). Additionally, in the mathematical model of the tear film dynamics with CL motion (Chauhan and Radke 2001; Anderson et al. 2021), CL thickness primarily influences the elastic force, which facilitates the centring of the CL on the cornea by affecting tear film dynamics. Although elastic energy per unit area is directly related to CL thickness, the base curve (measured in mm) emerges as the more influential factor compared to thickness (measured in μm). However, it is not as impactful compared to CL diameter and Young's modulus, which markedly affect the interaction of the CL with the tear film.

The study advances understanding of CL design by incorporating findings from lubrication regimes (Dunn et al. 2013). It becomes evident that while the base curve and thickness of CLs modestly impact tear film dynamics, other factors such as lubrication regimes—boundary, hydrodynamic, and mixed—play significant roles in lens fitting and comfort. These insights call for a holistic approach in CL design and selection, balancing material properties, geometric dimensions, and individual user characteristics to optimise tear film stability and performance. This strategy is vital for enhancing tear film stability and overall lens efficacy, ensuring that designs accommodate the specific lubrication needs critical for maintaining ocular health and comfort.

The impact of CL parameters on PLTF dynamics necessitates calculating correlation sample size, obtained from the correlation coefficient alongside probabilities set for hypothesis testing and a 95% confidence level. The study reveals the varying necessity of sample sizes based on correlation strength with PLTF thickness across different

CL parameters (Hulley 2013; Kohn and Senyak 2024). For instance, a minimum correlation coefficient of 0.74 with CL diameter suggests a smaller required sample size of 12, confirmed by the adequacy of the study with 16 samples. In contrast, Young's modulus shows a minimum correlation coefficient of 0.512, necessitating 28 samples to ensure significant results, hinting at nearly significant current observations. The base curve parameter displays a weaker correlation, indicating the need for 158 samples to achieve reliable significance, underscoring its limited impact on PLTF thickness. Additionally, the minimal correlation of 0.048 with CL thickness implies a vast requirement of 3404 samples, highlighting its negligible effect within practical limits. Given the high sample size demands, particularly for base curve and thickness parameters, which exceed the feasibility of testing multiple CL brands on a single subject, bootstrap sampling is proposed as a practical solution (Berrar and Dubitzky 2013; The MathWorks Inc. 2023c). This resampling technique uses existing data to generate multiple samples, effectively approximating larger datasets without extensive sample collection.

Bootstrap sampling was applied to explore the relationships between Young's modulus, base curve, and thickness of CL with PLTF thickness. For Young's modulus, bootstrap sampling was performed with more than 28 samples, determined from the correlation sample size calculations. The PDF of approximately 200 resampled correlation coefficients is depicted in Fig. 7, illustrating the distribution and variability of these coefficients. This visualization provides valuable insights into the density and consistency of the estimated correlations across the resampled data. Table 8 further presents the mean, standard deviation, and 95% confidence interval for the correlation coefficients between Young's modulus and mean PLTF thickness during the three phases of the blink cycle: upstroke, eye fully open, and downstroke.

For the CL base curve, the bootstrap sampling approach was extended to calculate the Pearson correlation coefficient between the base curve and mean PLTF thickness for more than 158 samples. Figure 8 illustrates the kernel density estimate for 200 samples, offering a smoothed probability density and a visual representation of the variability of the correlation coefficients across the blink cycle phases. Similarly, for CL thickness, the bootstrap sampling was performed with 4000 resamples, and Fig. 9 shows the kernel density estimate for these samples, providing another smoothed probability density and a detailed visualization of the variability in correlation coefficients during upstroke, eye fully open, and downstroke phases. Table 8 also includes the mean, standard deviation, and 95% confidence interval for the correlation coefficients between the CL parameters and mean PLTF thickness obtained from bootstrap sampling across all three phases.

The combined analysis of correlations presented in Table 8 and Figs. 7, 8, and 9 clarifies the significance of the relationships between CL parameters and PLTF thickness. A primary objective of this study is to identify which CL parameters most significantly influence tear film thickness. As an initial step, it is crucial to evaluate whether the correlations are predominantly positive or negative. Using the probability distributions of the correlation coefficients generated through the bootstrap procedure, the probabilities for these values are estimated, as shown in Table 9.

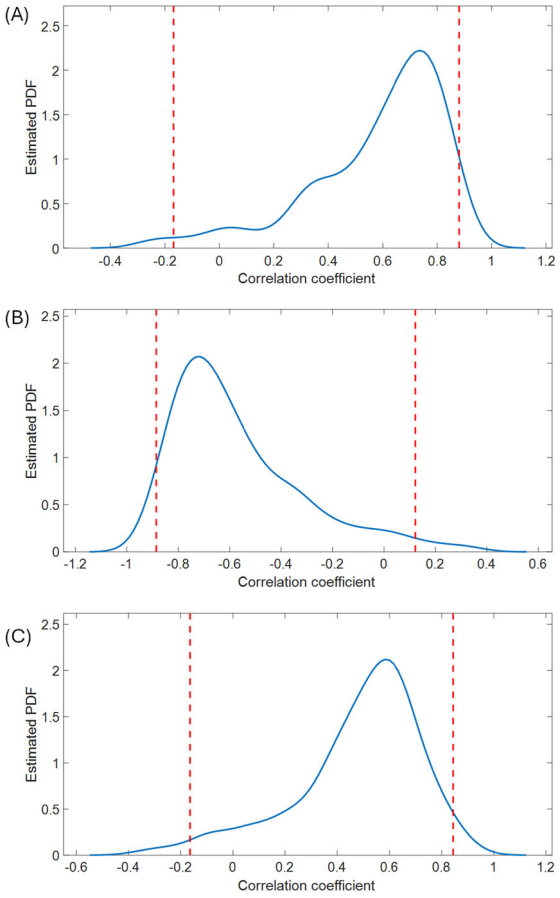

Fig. 7 Kernel density estimate of the correlation coefficient between CL Young's modulus and mean PLTF thickness, after the bootstrap sampling approach is applied with a sample size of 200 (more than 28 correlation sample size). **a** Upstroke phase, **b** Eye fully open, **c** Downstroke phase of the blink cycle

The analysis confirms that significant correlations were observed only with Young's modulus, as highlighted in Table 5 of the manuscript. Table 9 further supports this finding, indicating a high probability of consistent results through the bootstrap method. Conversely, for the other parameters, such as CL thickness and base curve, the bootstrap results show no clear distinction between positive or negative correlations, aligning with the non-significant statistical results ($p > 0.05$). Additionally, the sample size required to achieve significance for these parameters is impractically large, making it unfeasible in clinical scenarios. Therefore, Young's modulus emerges as the most relevant parameter influencing PLTF thickness. In contrast, the base curve and thickness parameters have limited impact and may instead be selected based on other considerations, such as wearer comfort. Furthermore, the variability of these parameters in commercially available CLs is relatively limited, further reducing their practical significance.

A limitation of this study is that the computational model is tested using sixteen CL parameters for only a single subject. This narrow scope may not capture the full variability in tear film dynamics and CL interactions across a diverse population.

Table 8 Summary of the mean, standard deviation, and 95% confidence interval of correlation coefficients for CL parameters (Young's modulus and base curve) and mean PLTF thickness across the three phases of the blink cycle: upstroke, eye fully open, and downstroke

CL Para-meters	Upstroke			Eye fully open			Downstroke		
	Mean ± Std	95% confidence interval		Mean ± Std	95% confidence interval		Mean ± Std	95% confidence interval	
		Lower bound	Upper bound		Lower bound	Upper bound		Lower bound	Upper bound
Young's modulus	0.584 ± 0.247	−0.168	0.880	−0.570 ± 0.256	−0.886	0.122	0.479 ± 0.241	−0.164	0.844
Base curve	−0.260 ± 0.245	−0.797	0.342	0.196 ± 0.239	−0.349	0.706	−0.323 ± 0.234	−0.777	0.222
Thick-ness	−0.052 ± 0.158	−0.361	0.282	−0.059 ± 0.166	−0.401	0.260	−0.271 ± 0.142	−0.543	0.014

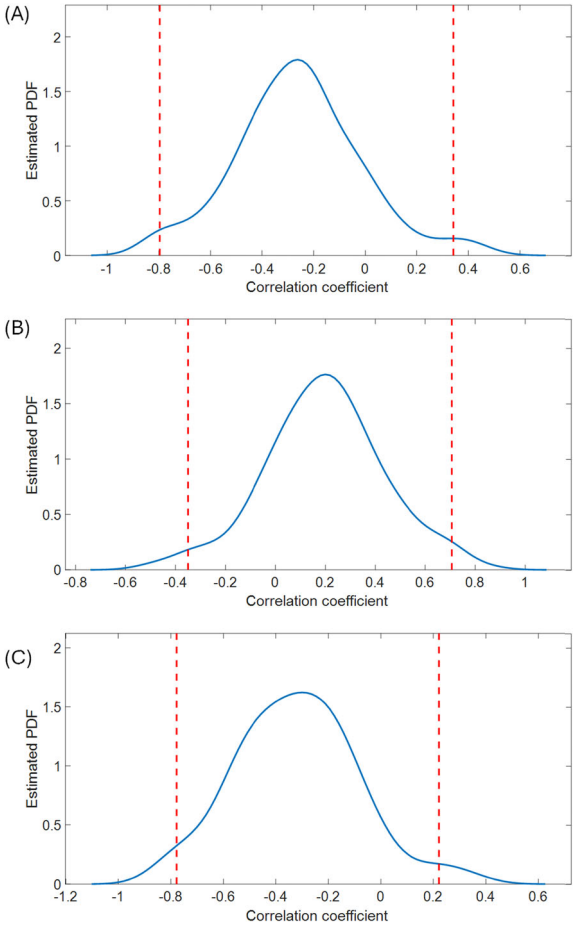

Fig. 8 Kernel density estimate of the correlation coefficient between CL base curve and mean PLTF thickness, after the bootstrap sampling approach is applied with a sample size more than 158 (obtained from correlation sample size). **a** Upstroke phase, **b** Eye fully open, **c** Downstroke phase of the blink cycle

Extending the model to include data from multiple subjects would enhance the robustness and generalizability of the findings, offering a more comprehensive understanding of comfort and effectiveness in CL wear. Additionally, integrating these models into a Multiphysics approach, combined with a biomechanical model of the human eye, could further refine the accuracy and applicability of the results, ultimately contributing to more personalised and effective CL designs.

5 Conclusion

The study employed mathematical models to investigate the dynamics of the tear film in relation to various CL parameters, revealing the significant roles of CL diameter and the material stiffness, as indicated by Young's modulus, in influencing tear film behaviour throughout the blink cycle. While the base curve and CL thickness were found to have a minor impact, the diameter and material stiffness significantly affect

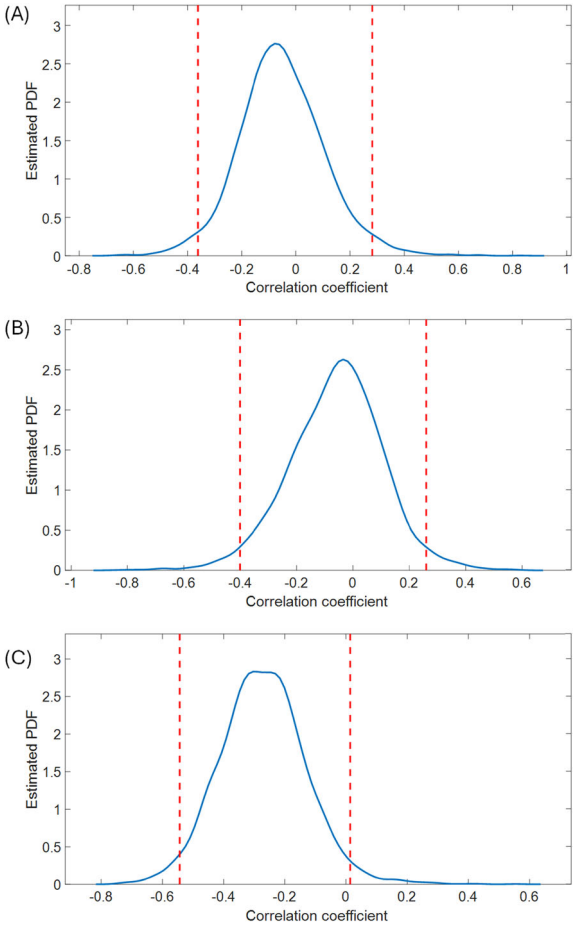

Fig. 9 Kernel density estimate of the correlation coefficient between CL thickness and mean PLTF thickness, after the bootstrap sampling approach is applied with a sample size of 4000 (greater than the correlation sample size of 3404). **a** Upstroke phase, **b** Eye fully open, **c** Downstroke phase of the blink cycle

Table 9 Probability of positive and negative correlation coefficient between CL parameters and tear film thickness from bootstrap estimation and for different moments of blink cycle

CL parameters	Upstroke		Eye fully open		Downstroke	
	Positive correlation (%)	Negative correlation (%)	Positive correlation (%)	Negative correlation (%)	Positive correlation (%)	Negative correlation (%)
Youngs' modulus	95.57	4.43	4.66	95.34	93.65	6.35
Base curve	13.59	86.41	78.20	21.80	8.10	91.90
Thickness	33.38	66.62	33.21	66.79	2.98	97.02

tear film stability, thickness, and distribution. These findings align with contemporary research, suggesting that optimal CL design should transcend conventional parameters and advocate for a personalised selection process. This process should consider a combination of material properties, geometric dimensions, and individual wearer characteristics to foster tear film stability and enhance lens performance. This study adopts an integrated approach to CL design, stressing the need for nuanced strategies tailored to individual wearers to enhance comfort, optimise performance, and promote ocular health. Expanding this research to include multiple subjects will improve the generalizability and applicability of the findings, further aiding the development of personalised and effective CL designs.

Funding This work is done as part of the European EYE project and the project has received funding from the European Union's Horizon 2020 research and innovation program under the Marie Skłodowska-Curie grant agreement No 956274. Grant Holder: Darshan Ramasubramanian.

Data Availability The manuscript has not associated data since is based on simulations and computational models. All the details to run the simulations are included in the manuscript with all the parameters and sample used. Authors can be contacted, anyway upon reasonable request.

AI Tools No AI tools were used in any part of the present work.

Declarations

Conflict of interest No conflicts of Interest.

Ethical Approval This study is conducted in strict accordance with the principles of the Declaration of Helsinki. Approval was granted by the Ethics Committee of Complutense University of Madrid, Madrid, Spain on June 7th, 2023. Written informed consent from participants was obtained prior to study commencement.

Consent for Publication Not applicable.

References

Anderson DM, Corsaro M, Horton J et al (2021) Tear film dynamics with blinking and contact lens motion. Math Med Biol J IMA 38:355–395. https://doi.org/10.1093/imammb/dqab010

Berrar D, Dubitzky W (2013) Bootstrapping. In: Dubitzky W, Wolkenhauer O, Cho K-H, Yokota H (eds) Encyclopedia of systems biology. Springer, New York, New York, NY, pp 158–162

Bowman AW, Azzalini A (1999) Applied smoothing techniques for data analysis: the kernel approach with s-plus illustrations. J Am Stat Assoc 94:982

Braun RJ (2003) Modelling drainage of the precorneal tear film after a blink. Math Med Biol 20:1–28. https://doi.org/10.1093/imammb/20.1.1

Braun RJ (2012) Dynamics of the tear film. Annu Rev Fluid Mech 44:267–297. https://doi.org/10.1146/annurev-fluid-120710-101042

Braun RJ, King-Smith PE (2007) Model problems for the tear film in a blink cycle: single-equation models. J Fluid Mech 586:465–490. https://doi.org/10.1017/S002211200700701X

Braun RJ, King-Smith PE, Begley CG et al (2015) Dynamics and function of the tear film in relation to the blink cycle. Prog Retin Eye Res 45:132–164. https://doi.org/10.1016/j.preteyeres.2014.11.001

Capote-Puente R, Bautista-Llamas M-J, Sánchez-González J-M (2023) Tear film dynamics between low and high contact lens dry eye disease questionnaire (CLDEQ-8) score with a Lehfilcon A silicone hydrogel water gradient contact lens: a non-invasive methodology approach. Diagnostics 13:939. https://doi.org/10.3390/diagnostics13050939

Chauhan A, Radke CJ (2001) Modeling the vertical motion of a soft contact lens. Curr Eye Res 22:102–108. https://doi.org/10.1076/ceyr.22.2.102.5521
Dunn AC, Tichy JA, Urueña JM, Sawyer WG (2013) Lubrication regimes in contact lens wear during a blink. Tribol Int 63:45–50. https://doi.org/10.1016/j.triboint.2013.01.008
Espinosa J, Domenech B, Vázquez C et al (2018) Blinking characterization from high speed video records. Application to biometric authentication. PLoS ONE 13:e0196125. https://doi.org/10.1371/journal.pone.0196125
Fink BA, Hill RM, Carney LG (1992) Influence of rigid contact lens base curve radius on tear pump efficiency. Optom vis Sci 69:60
Garhöfer G, Dos Santos VA, Stegmann H et al (2020) The association between tear film thickness as measured with OCT and symptoms and signs of dry eye disease: a pooled analysis of 6 clinical trials. JCM 9:3791. https://doi.org/10.3390/jcm9113791
Hart SM, McGhee EO, Urueña JM et al (2020) Surface gel layers reduce shear stress and damage of corneal epithelial cells. Tribol Lett 68:106. https://doi.org/10.1007/s11249-020-01344-3
Heryudono A, Braun RJ, Driscoll TA et al (2007) Single-equation models for the tear film in a blink cycle: realistic lid motion. Math Med Biol 24:347–377. https://doi.org/10.1093/imammb/dqm004
Hsiao C-J, Tung H-C, Tien C et al (2023) The influence of large-diameter multifocal contact lens on ocular surface, visual quality, and visual function for presbyopic adults with dry eye syndromes. Sci Rep 13:19444. https://doi.org/10.1038/s41598-023-46732-6
Hulley SB (ed) (2013) Designing clinical research, 4th edn. Wolters Kluwer/Lippincott Williams & Wilkins, Philadelphia
Iyamu E, Enobakhare O (2019) pH and osmolality of pre-corneal tear film and commercially available artificial tears
Jones MB, Please CP, McElwain DLS et al (2005) Dynamics of tear film deposition and draining. Math Med Biol J IMA 22:265–288. https://doi.org/10.1093/imammb/dqi012
Jones MB, Fulford GR, Please CP et al (2008) Elastohydrodynamics of the eyelid wiper. Bull Math Biol 70:323–343. https://doi.org/10.1007/s11538-007-9252-7
Kaur P, Stoltzfus J, Yellapu V (2018) Descriptive statistics. Int J Acad Med 4:60. https://doi.org/10.4103/IJAM.IJAM_7_18
Kim H-Y (2013) Statistical notes for clinical researchers: assessing normal distribution (2) using skewness and kurtosis. Restor Dent Endod 38:52. https://doi.org/10.5395/rde.2013.38.1.52
Kim E, Saha M, Ehrmann K (2018) Mechanical properties of contact lens materials. Eye Contact Lens Sci Clin Pract 44:S148–S156. https://doi.org/10.1097/ICL.0000000000000442
King-Smith E, Fink B, Hill R et al (2004) The thickness of the tear film. Curr Eye Res 29:357–368. https://doi.org/10.1080/02713680490516099
Kohn MA, Senyak J (2024) Sample size calculators for designing clinical research—correlation sample size. https://www.sample-size.net/. Accessed 9 Nov 2024
Kosloff D, Tal-Ezer H (1993) A Modified chebyshev Pseudospectral method with an O(N-1) time step restriction. J Comput Phys 104:457–469. https://doi.org/10.1006/jcph.1993.1044
Kwon K-A, Shipley RJ, Edirisinghe M et al (2013) High-speed camera characterization of voluntary eye blinking kinematics. J R Soc Interface 10:20130227. https://doi.org/10.1098/rsif.2013.0227
Lee W-H, Seo J-M, Hwang J-M (2017) The analysis of eye blinking pattern using high-frame-rate camera. 2017 39th annual international conference of the IEEE engineering in medicine and biology society (EMBC). IEEE, Seogwipo, pp 1509–1512
Lee JH, Kim CH, Choe CM, Choi TH (2020) Correlation analysis between ocular surface parameters with subjective symptom severity in dry eye disease. Korean J Ophthalmol 34:203–209. https://doi.org/10.3341/kjo.2019.0133
Lo'pez-Alonso JM (2002) Bad pixel identification by means of principal components analysis. Opt Eng 41:2152. https://doi.org/10.1117/1.1497397
López-Alonso JM, Alda J, Bernabéu E (2002) Principal-component characterization of noise for infrared images. Appl Opt 41:320. https://doi.org/10.1364/AO.41.000320
Maki KL, Ross DS (2014) A new model for the suction pressure under a contact lens. J Biol Syst 22:235–248. https://doi.org/10.1142/S021833901440004X
Martin DK, Holden BA (1986) Forces developed beneath hydrogel contact lenses due to squeeze pressure. Phys Med Biol 31:635–649. https://doi.org/10.1088/0031-9155/31/6/005
Mas D, Domenech B, Espinosa J et al (2010) Noninvasive measurement of eye retraction during blinking. Opt Lett 35:1884. https://doi.org/10.1364/OL.35.001884

McNamara NA, Polse KA, Brand RJ et al (1999) Tear mixing under a soft contact lens: effects of lens diameter. Am J Ophthalmol 127:659–665. https://doi.org/10.1016/S0002-9394(99)00051-3
Miot HA (2018) Correlation analysis in clinical and experimental studies. J Vasc Bras 17:275–279. https://doi.org/10.1590/1677-5449.174118
Muntz A, Subbaraman LN, Sorbara L, Jones L (2015) Tear exchange and contact lenses: a review. J Optom 8:2–11. https://doi.org/10.1016/j.optom.2014.12.001
Ng SC (2017) Principal component analysis to reduce dimension on digital image. Proc Comput Sci 111:113–119. https://doi.org/10.1016/j.procs.2017.06.017
Nichols JJ, King-Smith PE (2003) Thickness of the pre- and post-contact lens tear film measured in vivo by interferometry. Invest Ophthalmol vis Sci 44:68. https://doi.org/10.1167/iovs.02-0377
Nichols JJ, King-Smith PE (2004) The impact of hydrogel lens settling on the thickness of the tears and contact lens. Invest Ophthalmol vis Sci 45:2549. https://doi.org/10.1167/iovs.04-0149
Paranjpe V, Phung L, Galor A (2019) The tear film: anatomy and physiology. In: Guidoboni G, Harris A, Sacco R (eds) Ocular fluid dynamics. Springer International Publishing, Cham, pp 329–345
Parzen E (1962) On estimation of a probability density function and mode. Ann Math Stat 33:1065–1076
Perez J, Espinosa J, Domenech B et al (2011) Blinking kinematics description through non-invasive measurement. J Mod Opt 58:1857–1863. https://doi.org/10.1080/09500340.2011.554898
Raj A (2016) Anterior segment optical coherence tomography for tear meniscus evaluation and its correlation with other tear variables in healthy individuals. JCDR. https://doi.org/10.7860/JCDR/2016/18717.7722
Sanjuán AM, López-Alonso JM (2021) Caracterización de movimientos oculares mediante flujo óptico velocimétrico. In: Sampedro AG, Gimeno IB, Cobija MJL, et al (eds) Temas actuales en optometría SIYO 2021. Universidad de Valencia, pp 45–55
Saravanan C (2010) Color image to grayscale image conversion. 2010 second international conference on computer engineering and applications. IEEE, Bali Island, Indonesia, pp 196–199
Schober P, Boer C, Schwarte LA (2018) Correlation coefficients: appropriate use and interpretation. Anesth Analg 126:1763–1768. https://doi.org/10.1213/ANE.0000000000002864
Shampine LF, Reichelt MW (1997) The MATLAB ODE suite. SIAM J Sci Comput 18:1–22. https://doi.org/10.1137/S1064827594276424
Stapleton F, Tan J (2017) Impact of contact lens material, design, and fitting on discomfort. Eye Contact Lens Sci Clin Pract 43:32–39. https://doi.org/10.1097/ICL.0000000000000318
The MathWorks Inc. (2021) MATLAB version: 23.2.0.2459199 (R2023b). https://www.mathworks.com. Accessed 8 Nov 2023
The MathWorks Inc. (2023a) Kernel Distribution—MATLAB & Simulink. https://www.mathworks.com/help/stats/kernel-distribution.html. Accessed 24 Apr 2024
The MathWorks Inc. (2023b) Kernel smoothing function estimate for univariate and bivariate data—MATLAB ksdensity. https://www.mathworks.com/help/stats/ksdensity.html#References. Accessed 8 Aug 2024
The MathWorks Inc. (2023) Correlation coefficients—MATLAB corrcoef. https://www.mathworks.com/help/stats/corr.html?s_tid=doc_ta. Accessed 24 Apr 2024
The MathWorks Inc. (2023c) Bootstrap Sampling—MATLAB bootstrp. https://www.mathworks.com/help/stats/bootstrp.html#mw_cdd50063-8fd8-41ed-af6f-c53071293b4f. Accessed 5 Nov 2024
Thielicke W, Stamhuis EJ (2014) PIVlab—towards user-friendly, affordable and accurate digital particle image velocimetry in MATLAB. J Open Res Softw 2:30. https://doi.org/10.5334/jors.bl
Tiffany JM (1991) The viscosity of human tears. Int Ophthalmol 15:371–376. https://doi.org/10.1007/BF00137947
Tiffany JM, Winter N, Bliss G (1989) Tear film stability and tear surface tension. Curr Eye Res 8:507–515. https://doi.org/10.3109/02713688909000031
Trefethen LN (2000) Spectral methods in MATLAB. Society for Industrial and Applied Mathematics, Oxford, England
Upadhyaya A, Khan S, Sahay P et al (2020) Pentacam—a corneal tomography system. Delhi J Ophthalmol 31:90
Wang J, Fonn D, Simpson TL, Jones L (2003) Precorneal and pre- and postlens tear film thickness measured indirectly with optical coherence tomography. Invest Ophthalmol vis Sci 44:2524. https://doi.org/10.1167/iovs.02-0731
William Thielicke (2021a) PIVlab—particle image velocimetry (PIV) tool with GUI. https://pivlab.blogspot.com/. Accessed 9 Nov 2023a

William Thielicke (2021b) PIVlab—Digital Particle Image Velocimetry Tool for MATLAB. https://in.mathworks.com/matlabcentral/fileexchange/27659-pivlab-particle-image-velocimetry-piv-tool-with-gui. Accessed 9 Nov 2023b

Young G, Hall L, Sulley A et al (2017) Inter-relationship of soft contact lens diameter, base curve radius, and fit. Optom vis Sci 94:458–465. https://doi.org/10.1097/OPX.0000000000001048